Author Manuscript

Author Manuscript

Author Manuscript

Author Manuscript

HHS Public Access

Author manuscript

Nat Genet. Author manuscript; available in PMC 2018 August 19.

Published in final edited form as:

Nat Genet. 2018 March ; 50(3): 460–471. doi:10.1038/s41588-018-0054-7.

A CRISPR-based screen for Hedgehog signaling provides insights into ciliary function and ciliopathies

David K. Breslow[1,2,7,*], **Sascha Hoogendoorn**[3,7], **Adam R. Kopp**[2], **David W. Morgens**[4], **Brandon K. Vu**[2], **Margaret C. Kennedy**[1], **Kyuho Han**[4], **Amy Li**[4], **Gaelen T. Hess**[4], **Michael C. Bassik**[4], **James K. Chen**[3,5,*], and **Maxence V. Nachury**[2,6,*]

[1]Department of Molecular, Cellular and Developmental Biology, Yale University, New Haven, Connecticut, USA

[2]Department of Molecular and Cellular Physiology, Stanford University School of Medicine, Stanford, California, USA

[3]Department of Chemical and Systems Biology, Stanford University School of Medicine, Stanford, California, USA

[4]Department of Genetics, Stanford University School of Medicine, Stanford, CA 94305

[5]Department of Developmental Biology, Stanford University School of Medicine, Stanford, California, USA

Abstract

The primary cilium organizes Hedgehog signaling and shapes embryonic development, and its dysregulation is the unifying cause of ciliopathies. We conducted a functional genomic screen for Hedgehog signaling by engineering antibiotic-based selection of Hedgehog-responsive cells and applying genome-wide CRISPR-mediated gene disruption. The screen robustly identifies factors required for ciliary signaling with few false positives or false negatives. Characterization of hit genes uncovers novel components of several ciliary structures, including a protein complex containing δ- and ε-tubulin that is required for centriole maintenance. The screen also provides an unbiased tool for classifying ciliopathies and reveals that many congenital heart disorders are caused by loss of ciliary signaling. Collectively, our study enables a systematic analysis of ciliary

Users may view, print, copy, and download text and data-mine the content in such documents, for the purposes of academic research, subject always to the full Conditions of use: http://www.nature.com/authors/editorial_policies/license.html#terms

[*]Correspondence: David K. Breslow david.breslow@yale.edu (203) 432-8280. James K. Chen jameschen@stanford.edu (650) 725-3582. Maxence V. Nachury maxence.nachury@ucsf.edu (415) 476-6758.

[6]Present address: Department of Ophthalmology, UCSF, San Francisco, California, USA

[7]Co-first author

Competing financial interests

The authors declare no competing financial interests.

Author Contributions

D.K.B., S.H., J.K.C., and M.V.N. conceived the project with advice from M.C.B. D.K.B. and S.H. developed the Hh pathway reporter screening strategy with assistance from B.K.V. D.W.M., K.H., A. L., G.T.H, and M.C.B. provided functional genomics expertise, the genome-wide sgRNA library, and software for screen data analysis. D.K.B. conducted the genome-wide screen and screen data analysis with assistance from S.H. and A.R.K. D.K.B., S.H., A.R.K., and M.C.K. functionally characterized hit genes of interest, analyzed data, and prepared figures. D.K.B., S.H., J.K.C., and M.V.N. wrote the manuscript with assistance from M.C.B. D.K.B, S.H., G.T.H., M.C.B, J.K.C. and M.V.N. provided funding for the project.

Author Manuscript Author Manuscript Author Manuscript Author Manuscript

function and of ciliopathies and also defines a versatile platform for dissecting signaling pathways through CRISPR-based screening.

Keywords

CRISPR; functional genomics; primary cilium; signaling; Hedgehog; centriole; ciliopathy; genetic screen

Introduction

The primary cilium is a surface-exposed microtubule-based compartment that serves as an organizing center for diverse signaling pathways[1–3]. Mutations affecting cilia cause ciliopathies, a group of developmental disorders that includes Joubert Syndrome, Meckel Syndrome (MKS), Nephronophthisis (NPHP), and Bardet-Biedl Syndrome (BBS). The defining symptoms of ciliopathies include skeletal malformations, mental retardation, sensory defects, obesity, and kidney cysts and are thought to arise from misregulation of ciliary signaling pathways. Advances in human genetics have led to the identification of over 90 ciliopathy genes[4]. However, the molecular basis for many ciliopathy cases remains undiagnosed,[5] and critical aspects of cilium assembly and function remain poorly understood.

A leading paradigm for ciliary signaling is the vertebrate Hedgehog (Hh) pathway, which plays key roles in embryonic development and in cancers such as medulloblastoma and basal cell carcinoma[6,7]. Primary cilia are required for Hh signaling output[3], and all core components of the Hh signaling machinery – from the receptor PTCH1 to the GLI transcriptional effectors – dynamically localize to cilia during signal transduction.

Efforts to systematically identify genes needed for cilium assembly or Hh signaling have been reported, but these studies relied on arrayed siRNA libraries and exhibit the high rates of false positives and false negatives characteristic of such screens[8–11]. Recently, genome-wide screening using CRISPR/Cas9 for gene disruption has emerged as a powerful tool for functional genomics[12–15]. However, the pooled screening format used in these studies requires a means to select for/against or otherwise isolate cells exhibiting the desired phenotype, a requirement that has limited the scope of biological applications amenable to this approach. Indeed, most studies to date have searched for genes that either intrinsically affect cell growth or that affect sensitivity to applied perturbations[16–23].

Here, we engineered a Hh pathway-sensitive reporter to enable an antibiotic-based selection platform. Combining this reporter with a single guide RNA (sgRNA) lentiviral library targeting the mouse genome, we conducted a CRISPR-based screen that systematically identified ciliary components, Hh signaling machinery, and ciliopathy genes with few false positives or false negatives. We further show that previously uncharacterized hits encode new components of cilia and centrioles and also include novel ciliopathy genes.

Author Manuscript Author Manuscript Author Manuscript Author Manuscript

Results

Development of a Hh pathway reporter for pooled screening

Pooled functional screening requires the ability to enrich or deplete mutants that exhibit a desired phenotype. Because ciliary signaling is not intrinsically linked to such a selectable phenotype, we engineered a reporter that converts Hh signaling into antibiotic resistance (Fig. 1A–B). This transcriptional reporter was introduced into mouse NIH-3T3 fibroblasts, a widely used cell line for Hh signaling and cilium biology[24], and these cells were then modified to express Cas9-BFP (3T3-[Shh-BlastR;Cas9] cells).

To validate our reporter cell line, we virally introduced sgRNAs targeting regulators of the Hh pathway (Supplementary Table 1). The transmembrane receptor SMO and intraflagellar transport (IFT) complex subunit IFT88 are required for Hh signaling, while SUFU and GLI3 restrain Hh pathway activity (Fig. 1c, left). As expected, sgRNAs targeting *Smo* or *Ift88* severely reduced Sonic Hedgehog N-terminal domain (ShhN)-induced blasticidin resistance, while deleting *Gli3* potentiated blasticidin resistance and targeting *Sufu* led to ligand-independent blasticidin resistance (Fig. 1c, right). These effects on blasticidin resistance were paralleled by concordant changes in endogenous pathway outputs, including GLI1 expression and changes in GLI3 processing (Supplementary Fig. 1a). Additionally, Western blotting confirmed loss of target protein expression for *Gli3*, *Ift88*, and *Sufu* sgRNAs (Supplementary Fig. 1a,b).

We next tested the suitability of our reporter cells for pooled screening, which involves quantifying sgRNAs in blasticidin-selected and unselected cell pools to identify sgRNAs that confer a selective advantage or disadvantage (Fig. 1d). We mimicked screening conditions by mixing GFP-marked cells expressing a *Smo* sgRNA with mCherry-marked cells expressing a portion of our genome-wide sgRNA library. Flow cytometry revealed that the fraction of *Smo* sgRNA-transduced cells decreased by >12-fold and by >50-fold after one and two rounds of signaling and selection, respectively, thus indicating that our strategy is suitable for pooled screening (Fig. 1e,f).

Genome-wide screening

We conducted our genome-wide screen using a newly developed mouse sgRNA library[25]. Key features of this library are the use of 10 sgRNAs per gene and the inclusion of >10,000 negative control sgRNAs that are either non-targeting or that target “safe” sites with no predicted functional role (Supplementary Fig. 2a). We lentivirally transduced 3T3-[Shh-BlastR;Cas9] cells with this library at low multiplicity of infection and maintained sufficient cell numbers to ensure ~1000X coverage of the library. Cells were next exposed to ShhN for 24 h to fully stimulate Hh signaling, split into separate blastidicin-selected and unselected pools, and then subjected to a second cycle of signaling and selection before sgRNA quantification by deep sequencing (Fig. 1d). Genes affecting ciliary signaling were identified by comparing sgRNAs in the blastidicin-selected versus unselected cell pools, while genes affecting proliferation were identified by comparing the plasmid sgRNA library to the sgRNA population after 15 days growth in the absence of blasticidin. For statistical analysis, a maximum likelihood method termed casTLE[26] was used to determine a *P* value for each

Author Manuscript Author Manuscript Author Manuscript Author Manuscript

gene from the changes in sgRNA abundance. In addition, the casTLE method estimates the apparent strength of the phenotype (effect size) caused by knockout of a given gene.

Assessment of screen performance

We first assessed our ability to detect genes affecting growth. This readout is independent of our reporter-based selection strategy and enables comparisons to other proliferation-based screens. Using reference positive and negative essential gene sets[27], we found that our screen identified >90% of essential genes with a 5% false discovery rate (FDR) (Supplementary Fig. 2b and Supplementary Tables 2–3). This performance validates the design of our sgRNA library and is comparable to that seen with other recently described libraries[18,20].

We next evaluated the ability of our screen to identify genes known to participate in ciliary Hh signaling. Initial inspection of screen results for *Smo*, *Ift88*, *Gli1*, *Gli3*, and *Sufu* revealed several sgRNAs targeting each gene that were depleted or enriched as expected upon blasticidin selection (Fig. 2a). Virtually all known Hh signaling components were among the top hits, including positive regulators *Smo*, *Grk2*, *Kif7*, *Prkar1a*, *Gli1*, and *Gli2* and negative regulators *Ptch1*, *Adcy6*, *Gsk3b*, *Sufu*, and *Gli3* (Fig. 2b and Supplementary Table 4). Our screen also recovered hits that encompass nearly all functional and structural elements of cilia, highlighting the diverse features of cilia needed for signaling (Fig. 2c). For example, several hits encode components of the basal body that nucleates the cilium, the transition fibers that anchor the basal body to the cell surface, the transition zone that gates protein entry into the cilium, the motors that mediate intraciliary transport, and the IFT complexes that traffic ciliary cargos (Fig. 2c and Supplementary Table 4). We observed no apparent correlation between growth and signaling phenotypes, indicating that our antibiotic selection strategy is not biased by general effects on proliferation (Supplementary Fig. 2c).

In total, we obtained 472 hits at a 10% FDR and 969 hits at a 20% FDR, and 92% of these hits led to decreased rather than increased signaling (Fig. 2b). This asymmetry indicates that, under the saturating level of ShhN used here, many genes are required to sustain high-level signaling while fewer genes act to restrain pathway output. Gene ontology (GO) term analysis using DAVID[28] revealed that the top 472 hit genes were enriched for expected functional categories (e.g. cilium morphogenesis, $P = 9.6\times10^{-61}$; Smoothened signaling pathway, $P < 3.6\times10^{-32}$) as well as some novel categories, indicating new avenues for investigation (Fig. 2d and Supplementary Table 5). In some cases, corroborating reports support these new connections: mouse mutants for two hit genes that enable diphthamide modification exhibit Hh pathway-related phenotypes such as polydactyly[29,30], and *DPH1* mutations likewise cause a syndrome with ciliopathy-like features[31].

We next sought to use reference sets of expected hit and non-hit genes to quantitatively assess screen performance. We curated a set of ciliogenesis reference genes[8] to generate a list of 130 expected hits; for expected non-hits we used 1386 olfactory and vomeronasal receptor genes (Supplementary Table 3). We then calculated precision-recall and receiver operating characteristic (ROC) curves (Fig. 3a) from the *P* values generated by casTLE. Both performance metrics showed a high area under the curve (0.802 for precision-recall,

Author Manuscript Author Manuscript Author Manuscript Author Manuscript

0.892 for ROC), demonstrating that our screen detects hits with high sensitivity and precision (Fig. 3a).

As a second means of evaluation, we compared our ability to detect expected hit genes to that of three related screens. These studies used arrayed siRNA-based screening to study either Hh signaling using a luciferase reporter[10] or ciliogenesis using microscopy-based measures of ciliary markers[8,9]. While there are notable differences among the screens (e.g. Roosing et al. incorporated gene expression data to score hits[8]), they each defined a number of hit genes similar to our screen. Overall, we detected the vast majority of expected hits across functional categories ranging from Hh pathway components to ciliopathy genes. Furthermore, even though our screen was focused on Hh signaling, we detected a greater fraction of ciliary hits than the ciliogenesis screens across categories including IFT subunits, ciliary motors, and nearly all classes of ciliopathy genes (Fig. 3b,c, Supplementary Fig. 3a and Supplementary Table 4). Indeed, among the 88 genes encompassed by the categories shown in Fig. 3b (except for NPHP-specific genes; see below), we detect 65 as hits, indicating that our screen is approaching saturation (Fig. 3c). Interestingly, few hits were found for genes mutated exclusively in NPHP, raising the possibility that NPHP pathophysiology is distinct from that of other ciliopathies (see Supplementary Note).

As a final assessment of our screening platform, we evaluated reproducibility across replicate screens. We observed high concordance among hits for the 95 genes measured in two different batches of the screen, with 50 of 54 screen hits also scoring as hits in the second batch (Supplementary Fig. 3b). Similarly, strong overlap in hits was found for 263 genes that were screened using two similar but distinct activators of Hh signaling: PTCH1 ligand (ShhN) and SMO agonist (SAG) (Supplementary Fig. 3c). This reproducibility makes it possible to pinpoint genes acting at specific steps in Hh signal transduction. For example, *Gas1* was a hit in the ShhN screen but not in the SAG screen, a result in agreement with GAS1's known function as a Shh co-receptor[32,33].

Identification of new ciliary components

To further establish the value of our screen, we next set out to characterize six previously unstudied hit genes. We first focused on *Fam92a* and *Ttc23* because their gene products contain domains associated with membrane trafficking. For *Fam92a*, we generated mutant cell pools using individually cloned sgRNAs and confirmed by sequencing that most cells harbored likely null alleles[34]. Indeed, a high rate of mutagenesis was observed for all genes characterized here and below (Supplementary Fig. 4a). *Fam92a* disruption caused a strong defect in inducible blasticidin resistance (Supplementary Fig. 4b). This defect was also seen for induction of luciferase from a GLI binding site reporter and could be rescued by sgRNA-resistant *Fam92a* (Fig. 4a), indicating that the phenotype is specific and independent of the blasticidin-based readout. Notably, ciliogenesis was severely reduced in *Fam92a* knockout cell pools (Fig. 4b). To gain further insight into *Fam92a* function, we identified FAM92A-associated proteins from cells expressing FAM92A-LAP (S-tag-HRV3C-GFP localization and affinity purification tag). FAM92-LAP purification specifically recovered CBY1 and DZIP1L, which are components of the transition zone (Fig. 4c and Supplementary Table 6)[35–37]. Consistent with this finding, we observed FAM92A localization at the transition

Author Manuscript Author Manuscript Author Manuscript Author Manuscript

zone using a validated antibody (Supplementary Fig. 4c,d) and the FAM92A-LAP cell line (Fig. 4d). While this work was in progress, another group independently established FAM92A as a transition zone protein that interacts with CBY1 and promotes ciliogenesis[38].

To characterize the TPR domain-containing protein TTC23, we identified TTC23-interacting proteins by affinity purification and mass spectrometry. Notably, the most prominent TTC23-associated proteins were IQCE and EFCAB7, which localize to a proximal region of the cilium known as the Ellis-van Creveld (EvC) zone (Fig. 4e and Supplementary Table 6)[39,40]. While the four known EvC zone proteins are dispensable for cilium assembly, they are all important for Hh signaling. Furthermore, mutations that affect EvC zone proteins EVC and EVC2 cause the ciliopathy Ellis-van Creveld syndrome[39–41]. Consistent with TTC23 being a new EvC zone component, TTC23-LAP co-localized with EVC and IQCE at the EvC zone (Fig. 4f and Supplementary Fig. 4e). Although *Ttc23* knockout had no effect on cilium assembly, mutant cells exhibited decreased blasticidin resistance and reduced localization of IQCE and EVC to the EvC zone (Fig. 4g and Supplementary Fig. 4b,f–h). Conversely, *Iqce* RNAi led to decreased localization of TTC23-LAP to the EvC zone (Fig. 4h). Together these results establish TTC23 as a novel EvC zone component that participates in Hh signaling.

Identification of novel disease genes

Because the vast majority of ciliopathy genes were hits in the screen, we asked whether uncharacterized hit genes may be mutated in ciliopathies of previously unknown etiology. We first examined *Txndc15*, which encodes a thioredoxin domain-containing transmembrane protein. A previous analysis of MKS patients identified a family with a *TXNDC15* mutation; however, a coincident *EXOC4* variant was favored as the causative mutation[42]. We analyzed *Txndc15* knockout cells using the luciferase reporter assay, finding a clear defect in Hh signaling. Furthermore, wildtype *Txndc15* rescued this defect, whereas the mutant allele found in MKS patients behaved like a null allele (Fig. 5a). We also found that cilia in *Txndc15* knockout cells exhibited increased variability in length and decreased levels of the ciliary GTPase ARL13B (Fig. 5b and Supplementary Fig. 5a,b). Thus, *TXNDC15* likely represents a novel MKS gene. Consistent with our findings, a very recent follow-up study has identified additional MKS families with *TXNDC15* mutations and characterized ciliary defects resulting from *TXNDC15* disruption[43].

Our observation of *Armc9* as a screen hit raises the possibility that it is also a ciliopathy gene. Recently, Kar et al. reported that individuals with a homozygous mutation in *ARMC9* present with mental retardation, polydactyly, and ptosis, but a diagnosis of Bardet-Biedl syndrome was disfavored[44,45]. We found that cilia from *Armc9* mutant cells were short and exhibited reduced levels of acetylated and polyglutamylated tubulin (Fig. 5c and Supplementary Fig. 5c). Furthermore, ARMC9-3xFLAG localized to the proximal region of cilia when stably expressed in IMCD3 or NIH-3T3 cells (Fig. 5d,e and Supplementary Fig. 5d). Notably, stimulation of Hh signaling in IMCD3 cells led to redistribution of ARMC9 towards the ciliary tip within 6 hr before a gradual return to its original proximal location, suggesting that ARMC9 might become ectocytosed from the cilium tip at later time points[46,47] (Fig. 5d,e). This change in localization was due to Hh signaling, as it was

Author Manuscript Author Manuscript Author Manuscript Author Manuscript

blocked by SMO inhibitor vismodegib (Supplementary Fig. 5e). Furthermore, *Armc9* mutant NIH-3T3 cells exhibited reduced ciliary accumulation of GLI2 and GLI3 (but not SMO) upon pathway activation, suggesting that ARMC9 participates in the trafficking and/or retention of GLI proteins at the ciliary tip (Fig. 5f and Supplementary Fig. 5f–h). Collectively, these findings demonstrate that ARMC9 is a ciliary signaling factor and suggest that *ARMC9* is a novel ciliopathy gene. Indeed, a recent report confirms that *ARMC9* is mutated in Joubert Syndrome and finds that loss of the zebrafish ortholog disrupts cilium assembly and function[48]. This study further reports that ARMC9 localizes to centrioles in RPE cells, whereas we find ARMC9-FLAG localizes to cilia (Fig. 5d,e and Supplementary Fig. 5d) and is present in the ciliary proteome (D. Mick and M. Nachury, personal communication). While the basis for these differing observations warrants further investigation, together these data reveal an important role for ARMC9 in ciliary signaling.

Our evidence that *ARMC9*- (and *DPH1*-) based syndromes likely represent unrecognized ciliopathies led us to ask whether our screen could help classify other genetic disorders as ciliopathies. Consistent with this possibility, *CWC27*, which encodes a peptidyl-prolyl isomerase, and *INTS1* and *INTS8*, which encode subunits of the Integrator, are orthologues of screen hits for which patient mutations have recently been described[49]. Some canonical ciliopathy symptoms are present in these patients, and thus these disorders may stem from altered ciliary signaling (see Supplementary Note).

These cases of individual disorders that can now be classified as likely ciliopathies led us to ask whether systematic efforts to map disease genes might reveal broader commonalities with our screen hits. Strikingly, we found that human orthologues of screen hits *Ankrd11*, *Cdk13*, *Chd4*, *Foxp1*, *Kmt2d*, and *Prkd1* were all identified in an exome sequencing study of patients with congenital heart defects (CHD)[50,51]. The significant overlap in these two unbiased datasets ($P = 6.11 \times 10^{-4}$) indicates that defective ciliary signaling may be a prevalent cause of CHDs. Moreover, mutations in these genes appear to cause *bona fide* ciliopathies, as patients also exhibit ciliopathy symptoms including craniofacial abnormalities and developmental delay (*ANKRD11*, *CDK13*, *CHD4*, *FOXP1*, *KMT2D*, *PRKD1*), dysgenesis of the corpus callosum (*CDK13*), polydactyly (*CHD4*), obesity (*ANKRD11*), and craniofacial malformations (*ANKRD11* and *KMT2D*)[4,50,52] (Fig. 5g).

A new protein complex for centriole stability

Because our screen hits encode centriolar proteins CEP19, CEP44, CEP120, and CEP295[53–62], we considered whether other hits might also have centriolar functions. Indeed, the protein encoded by uncharacterized hit *1600002H07Rik* (human *C16orf59*) localized to centrioles in IMCD3 cells (Fig. 6a). We performed affinity purifications and found that 1600002H07Rik-LAP co-purified with the uncharacterized protein 4930427A07Rik (human C14orf80) and the distant α/β-tubulin relatives ε-tubulin (TUBE1) and δ-tubulin (TUBD1) (Fig. 6b). All four of the genes encoding these proteins are hits in our screen, and ε-tubulin and δ-tubulin have previously been linked to centriole assembly and maintenance[63–67]. We therefore propose to name *4930427A07Rik*/*C14orf80* and *1600002H07Rik*/*C16orf59* as *Tedc1* and *Tedc2*, respectively, for their association with a tubulins epsilon and delta complex.

Author Manuscript Author Manuscript Author Manuscript Author Manuscript

Our mass spectrometry analysis of TEDC2-associated proteins revealed approximately stoichiometric amounts of TEDC1, TEDC2, ε-tubulin, and δ-tubulin, as seen by comparison of the normalized spectral abundance factors (Fig. 6b and Supplementary Table 6). We also recovered lower amounts of α/β-tubulin and CENPJ, a centriolar regulator of microtubule dynamics[68–70]. We confirmed co-purification of TUBD1 and TUBE1 with TEDC2 by Western blot, readily detecting these proteins in our TEDC2-LAP purification but not in a control purification (Supplementary Fig. 6a). The interaction between TEDC1 and TEDC2 could also be detected by co-transfection and co-immunoprecipitation, and moreover we found that TEDC1 and TEDC2 mutually stabilize each other's expression (Fig. 6c and Supplementary Fig. 6b). In further support of our data, two large-scale proteomic datasets have also identified interactions among TED complex proteins[71,72].

To functionally characterize *Tedc1* and *Tedc2*, we examined mutant cell pools and found that they were almost completely devoid of centrioles, as assessed by staining with antibodies to centrin, ninein, polyglutamylated tubulin or γ-tubulin (Fig. 7a,c,d). Mutant cells also lacked cilia (Fig. 7a) and had strong defects in Hh signaling (Supplementary Fig. 6c,d). Notably, centrioles and cilia were restored in *Tedc1* mutant cells following introduction of sgRNA-resistant TEDC1-Flag (Supplementary Fig. 6e,f), which also localized to centrioles (Supplementary Fig. 6g).

We noted that *Tedc1* and *Tedc2* mutants exhibited a mild growth defect (Supplementary Table 3), which is consistent with recent evidence that NIH-3T3 cells lacking centrioles proliferate at a reduced rate[73]. By contrast, in other cell types, a p53-dependent arrest prevents growth in the absence of centrioles. These observations prompted us to investigate whether the varying effects of *Tedc1* or *Tedc2* on proliferation across different cell types could enable predictive identification of genes with similar function. We therefore examined a collection of CRISPR-based growth screens conducted in 33 different human cell lines and used hierarchical clustering to group genes based on their cell type-specific growth phenotypes[74]. Strikingly, this unbiased approach placed *TEDC1*, *TEDC2*, and *TUBE1* in a single cluster (Fig. 7b and Supplementary Table 7), suggesting that they share a highly similar function. While *TUBD1* was not found in this cluster, this result is likely due to ineffective targeting of *TUBD1* by the sgRNA library used. Indeed, while other CRISPR screens have reported pronounced growth defects for *TUBD1* mutants[18,25], this study did not.[74].

To better understand the basis for centriole loss in *Tedc1* and *Tedc2* mutants, we examined cells at different stages of the cell cycle. Surprisingly, while mutant cells typically had zero or one centriole in interphase, nearly all mitotic cells had excess centrioles (more than four), suggestive of *de novo* centriole formation before mitotic entry (Fig. 7c,d and Supplementary Fig. 6h). By contrast, cells exiting mitosis showed significantly fewer centrioles than control cells (Fig. 7d). Taken together, these observations suggest that *Tedc1* and *Tedc2* are dispensable for centriole biogenesis but required for centriole stability, with newly generated centrioles rapidly lost as cells exit mitosis. In further support of a shared function for TED complex components, *TUBE1*- and *TUBD1*-deficient human cells were recently shown to have a similar phenotype[75].

Author Manuscript Author Manuscript Author Manuscript Author Manuscript

Discussion

Here we present a functional screening platform that pairs a pathway-specific selectable reporter with genome-wide CRISPR-based gene disruption. Applying these technologies to cilium-dependent Hh signaling, we obtain a comprehensive portrait of cilium biology that identifies hit genes with high sensitivity and specificity. Several factors likely contributed to the quality of our screen, including the pooled screening format, the use of CRISPR for gene disruption, and a newly designed sgRNA library (see Supplementary Note). Furthermore, our use of a selectable pathway reporter makes this technology applicable to virtually any process with a well-defined transcriptional response.

Our pooled CRISPR-based screening approach enabled us to generate a rich dataset that will be a valuable resource for dissecting ciliary signaling, defining ciliopathy genes, and discovering potential therapeutic targets in Hh-driven cancers. While siRNA-based screens have contributed to our understanding of cilia and Hh signaling, these datasets suffer from false positives or false negatives that limit their utility. Roosing et al.[8] improved their ciliogenesis screen results by using reference gene sets to help classify hits and by integrating gene expression datasets with their microscopy-based screen data. Our approach achieved high performance without dependence on other data sources, which may not always be available, or on *a priori* definition of hits, which could bias discovery of new hit classes. Our screens are also highly reproducible, thereby enabling comparative screening approaches that will be instrumental in uncovering novel factors acting at specific steps in Hh signaling. Modifications to our screening strategy, such as performing screens in other cell lines or in unstimulated (or weakly stimulated) cells, may better replicate certain *in vivo* signaling modalities and may have improved sensitivity for identifying negative regulators of Hh signaling.

The value of our screen is demonstrated by the discovery of new genes that participate in ciliary signaling and new candidate ciliopathy genes. While the precise roles of FAM92A at the transition zone and TTC23 at the EvC zone will require further study, our screen demonstrates that new components remain to be identified even for well-studied ciliary structures. Similarly, our analyses of *TXNDC15*, *ARMC9*, *CWC27*, *DPH1*, *INTS6*, *INTS10*, *ANKRD11*, *CDK13*, *CHD4*, *FOXP1*, *PRKD1,* and *KTM2D* illustrate that screen hits can help to identify a ciliopathy-causing gene from a short list of variants, as is frequently the case in studies involving small pedigrees, and to classify new genetic syndromes as disorders of ciliary signaling. With the exception of *TXNDC15*, all of the aforementioned genes had been previously linked to disease without a potential role for cilia described (e.g. *KMT2D* and Kabuki Syndrome, OMIM 147920; *ANKRD11* and KBG Syndrome, OMIM 148050; *DPH1* and Loucks-Innes Syndrome, OMIM 616901). Among the syndromes caused by mutations in these genes, it is striking that the most prevalent feature is CHD. Our screen thus provides unbiased evidence that several CHD cases are ciliopathies, building upon similar connections observed in mice[76] and motivating future investigations by human geneticists and developmental biologists.

By contrast, it is noteworthy that few of the ciliopathy genes primarily linked to kidney pathology were found as screen hits, suggesting that these renal diseases are mechanistically

Author Manuscript Author Manuscript Author Manuscript Author Manuscript

distinct (see Supplementary Note). By capturing an unbiased picture of cilium-based signaling, our screen refines the classification of ciliopathies. More broadly, as genome sequencing reveals disease-associated variants at ever-growing rates, genome-wide functional studies such as that presented here will become a powerful resource to distinguish disease-causing mutations from innocuous variants[77] and to gain insight into underlying disease mechanisms.

Our screen identifies hit genes with diverse roles in cilium function, Hh signaling, and centriole biology. For hits *Tedc1*, *Tedc2*, *Tubd1*, and *Tube1*, we found that these genes act in concert to ensure centriole stability, as evidenced by the association of their gene products in a stoichiometric complex. This finding reveals a new direct link between ε- and δ-tubulin and raises the possibility that they may form a heterodimer analogous to α/β-tubulin. In addition to the physical association of TED complex components, deficiency for TED complex-encoding genes produces a remarkably similar pattern of growth phenotypes across cell lines. Moreover, we find that these genes exhibit a similar phylogenetic distribution (see Supplementary Table 8, Supplementary Fig. 7, and Supplementary Note). Together, these observations provide further evidence for a shared function and illustrate the precise functional predictions made possible by CRISPR-based growth profiling[18].

Studies in *Paramecium*, *Tetrahymena*, *Chlamydomonas reinhardtii*, and, most recently, human cells have shown that disrupting δ- or ε-tubulin leads to loss of the C and/or B tubules of the centriolar triplet microtubules[64,66,67,78]. We propose that the centrioles formed in *Tedc1/2*-deficient cells similarly lack triplet microtubules, causing them to degenerate during mitotic exit at the time when pericentriolar material (PCM) is stripped from the centrosome. Since removal of the PCM causes centriolar instability in fly spermatocytes[79], post-mitotic PCM removal may also trigger centriole loss in *Tedc1/2* mutants. CENPJ may act together with the TED complex to ensure centriole stability, as CENPJ was found in our TEDC2 purifications and a mutation in *Cenpj* disrupts triplet microtubules in *Drosophila* spermatocytes[80]. As *CENPJ* is a microcephaly gene[81,82], TED complex components are potential candidate genes for this neurodevelopmental disorder.

In summary, we have developed a functional screening platform that provides a resource for investigating long-standing questions in Hh signaling and primary cilia biology. By further applying these tools, it may now be possible to systematically define vulnerabilities in Hh pathway-driven cancers, to identify modifiers of Hh pathway-inhibiting chemotherapeutics, and to search for suppressors of ciliopathies that may inform treatment. Integrating this functional genomic approach with complementary insights from proteomics and human genetics promises a rich toolkit for understanding ciliary signaling in health and disease.

Online Methods

CONTACT FOR REAGENT AND RESOURCE SHARING

Further information and requests for resources and reagents should be directed to David Breslow (david.breslow@yale.edu).

Author Manuscript Author Manuscript Author Manuscript Author Manuscript

EXPERIMENTAL MODELS AND SUBJECT DETAILS

Cell lines and cell culture—NIH-3T3 and HEK293T cells were grown in high glucose, pyruvate-supplemented DMEM (Gibco) with 10% fetal bovine serum (FBS), 2 mM glutamine, 10 U/ml penicillin and 10 μg/ml streptomycin (Gemini Bio-Products). NIH-3T3 FlpIn cells (gift from R. Rohatgi) were grown in the same medium supplemented with non-essential amino acids (Gibco). Light-II NIH-3T3 cells[24] were grown in the same medium except with 10% bovine calf serum (ATCC), and IMCD3 cells were grown in DMEM/F12 medium (Gibco) with FBS, glutamine, penicillin and streptomycin additives. Serum starvation was done using medium with 0.5% FBS for NIH-3T3 cells, 0.5% calf serum for Light-II NIH-3T3 cells, and 0.2% FBS for IMCD3 cells. IMCD3 FlpIn cells were provided by Peter Jackson. NIH-3T3 cells were obtained from ATCC. HEK239T-EcR-ShhN cells were provided by Philip Beachy. Cells were confirmed to be mycoplasma free with the MycoAlert system (Lonza).

METHOD DETAILS

DNA cloning—Individual sgRNAs were cloned by ligating annealed oligonucleotides into pMCB306 or pMCB320 digested with BstXI and Bpu1102I (Fermentas FastDigest enzymes, Thermo Fisher). Ligated products were transformed into Mach1-T1 competent cells (Thermo Fisher), and recovered plasmids were verified by sequencing.

Cilia-focused sgRNA libraries were cloned from oligonucleotide pools (Agilent) as described[25]. Briefly, oligonucleotides were amplified using primer sequences common to each sub-library, digested with BstXI and Bpu1102I, ligated into pMCB320, and transformed into Endura competent cells (Lucigen). DNA was isolated using a Plasmid Plus Giga kit (Qiagen).

Individual cDNAs were amplified from mouse cDNA or commercially available sources (Dharmacon) and cloned into Gateway Entry vectors via BP clonase-mediated recombination (Thermo Fisher) or using isothermal assembly. Mutations to introduce resistance to sgRNA-directed cleavage were introduced by isothermal assembly. Plasmids for expression of tagged genes of interest were generated from Entry vectors by LR clonase-mediated recombination (Thermo Fisher) into Destination vectors encoding C-terminal LAP, 3xFLAG, or 6xMyc tags.

Plasmid pHR-Pgk-Cas9-BFP was cloned by digestion of pHR-SFFV-Cas9-BFP (M. Bassik) and replacement of the SFFV promoter with the Pgk promoter amplified from pEFB/FRT-pCrys-^{AP}Gpr161^{NG3}-NsiI-pPgk-BirA-ER[46]. Plasmid pGL-8xGli-Bsd-T2A-GFP-Hyg was generated in the pGL4.29-[luc2P/CRE/Hygro] vector (Promega) by replacement of the CRE response element with 8xGli binding sites amplified from pGL3-8xGli-Luc (P. Beachy) and of Luc2P with Bsd-T2A-GFP amplified from pEF5B-FRT-DEST-LAP[83].

Virus production and cell transduction—VSVG-pseudotyped lentiviral particles were produced by co-transfection of HEK293T cells with a lentiviral vector and appropriate packaging plasmids (pMD2.G, pRSV-Rev, pMDLg/RRE for sgRNAs expressed in pMCB320 or pMCB306; pCMV-ΔR-8.91 and pCMV-VSVG for Pgk-Cas9-BFP). Following

Author Manuscript Author Manuscript Author Manuscript Author Manuscript

transfection using polyethyleneimine (linear, MW~25000, Polysciences), virus-containing supernatant was collected 24 h later and filtered through a 0.45 μm cellulose acetate filter. For sgRNA libraries, a second harvest of viral medium was performed 24 h after the initial harvest. For Cas9-containing virus, lentiviral particles were concentrated 20-fold using Lenti-X Concentrator (Clontech).

Cells were transduced by addition of viral supernatants diluted to an appropriate titer in growth medium containing 4 μg/ml polybrene (Sigma Aldrich). Following 24 h incubation at 37°C, virus-containing medium was removed; after an additional 24 h, cells were passaged and, where appropriate, selection for transduced cells was commenced by addition of 2.0 μg/ml puromycin (Invivogen). Multiplicity of infection was determined by flow cytometry.

ShhN production and titering—ShhN-containing conditioned medium was produced in HEK239T-EcR-ShhN cells. Cells were grown to 80% confluence, medium changed to DMEM with 2% FBS, followed by collection of conditioned medium after 48 h and filtration through a 0.22 μm filter (EMD Millipore). The titer of ShhN was determined using NIH-3T3 Light-II reporter cells (see *Luciferase reporter assays*), and a concentration approximately two-fold greater than the minimum dilution needed for full induction was used for further experiments (typically 1:12.5).

Flow cytometry and fluorescence-activated cell sorting—Flow cytometry analyses were conducted using a FACSScan (Becton Dickinson) outfitted with lasers provided by Cytek Biosciences. FACS was performed using FACSAria II cell sorters (Becton Dickinson). Flow cytometry and FACS data were analyzed using Flowjo (Treestar).

Generation of stable cell lines—The 3T3-[Shh-BlastR;Cas9] reporter cell line was generated using Lipofectamine 2000 (Thermo Fisher) to transfect NIH-3T3 cells with pGL-8xGli-Bsd-T2A-GFP-Hyg. Following selection for hygromycin-resistant cells, clonal isolates were obtained by limiting dilution and tested for SAG-induced blastidicin resistance. Pgk-Cas9-BFP was introduced lentivirally, followed by three rounds of FACS sorting for high-level BFP expression.

Stable cell lines for affinity purification and localization studies were generated using the FlpIn system (Life Technologies) with IMCD3 FlpIn or NIH-3T3 FlpIn cells. Plasmids encoding genes of interest in the pEF5B/FRT-DEST-LAP (or 3xFLAG) vector were transfected into FlpIn cells together with pOG44 Flp recombinase (Life Technologies) using X-tremegene 9 (Roche). Recombined cell pools were obtained following selection with blasticidin (Sigma Aldrich).

Rescue of *Tedc1* mutant cells was performed by lentiviral transduction with a construct expressing sgRNA-resistant mouse TEDC1-3xFlag-T2A-GFP. This construct was expressed from the Pgk promoter, and cells were analyzed 7–14 days post-transduction.

Blasticidin reporter assays—3T3-[Shh-BlastR;Cas9] cells were seeded for signaling and grown to near confluence. Growth medium was replaced with serum starvation medium with or without pathway agonist (ShhN conditioned medium or 250 nM SAG, synthesized

Author Manuscript Author Manuscript Author Manuscript Author Manuscript

as described[84,85]). After 24 h, cells were passaged at ~1:6 dilution into medium with 10% FBS, and 5 h later subjected to selection with blasticidin (blasticidin S hydrochloride, Sigma Aldrich) for 4 d. Relative viability was determined using the CellTiter-Blue assay (Promega) using a SpectraMax Paradigm (Molecular Devices) or Infinite M1000 (Tecan) plate reader.

Genome-wide screening—Due to the large number of cells required, we conducted the screen in four batches using subsets of the library containing ~45,000–70,000 sgRNAs (Supplementary Fig. 2a)[25]. For each batch, lentivirus was produced and titered as described above. 3T3-[Shh-BlastR;Cas9] cells were grown in 15 cm plates and transduced at a multiplicity of infection of ~0.3 in sufficient numbers such that there was a ~500:1 ratio of transduced cells to sgRNA library elements. Cells were selected with puromycin for 5 d, grown for 3 d without puromycin, and then plated for signaling, maintaining a ~1,000:1 ratio of cells to sgRNAs for these and all subsequent steps. After cells reached confluence, signaling was initiated by addition of serum starvation medium containing ShhN. After 24 h, cells were passaged, allowed to adhere, and then subjected to blasticidin selection for 4 d at 5 μg/ml, a concentration we found sufficient to achieve strong enrichment/depletion of hits without causing sgRNA library bottlenecks due to excess cell death. After passaging cells to blasticidin-free medium, a 'T1' sample was harvested (1000-fold more cells than sgRNAs) and remaining cells were passaged once more before seeding for a second round of signaling and selection. The final 'T2' cell sample was collected following 4 d blasticidin selection and one additional passage in the absence of blasticidin. Unselected control cells were also propagated through the entire experiment and harvested at equivalent timepoints.

Screens using the cilia/Hh pathway-focused library were conducted as above except that a variant blasticidin reporter cell line was used in which Cas9-BFP was expressed using the shortened EF1α promoter. Because some Cas9-negative cells accumulated during the experiment, the final blasticidin-selected and unselected cells were FACS-sorted for BFP expression.

To process cell samples for sgRNA sequencing, genomic DNA was isolated using QiaAmp DNA Blood Maxi or QiaAmp DNA mini kits (Qiagen). Genomic DNA was then amplified using Herculase II polymerase (Agilent) as described[16], first using outer primers to amplify the sgRNA cassette, then inner primers to amplify a portion of the initial PCR product while introducing sample-specific barcodes and adapters for Illumina sequencing (Supplementary Table 9). Gel-purified PCR products were quantified with a Qubit 2.0 fluorometer using the dsDNA HS kit (Thermo Fisher) and pooled for sequencing. Deep sequencing was performed on a NextSeq 500 sequencer with high-output v2 kits (Illumina) to obtain ~500-fold excess of reads to sgRNA library elements. Sequencing was performed using a custom primer to read the sgRNA protospacer (see Supplementary Table 9).

Cas9-induced mutation analysis by sequencing—Genomic DNA from sgRNA-transduced cell pools was extracted using the QIAamp DNA Mini kit (Qiagen) and amplified using primers flanking the sgRNA target site (see Supplementary Table 1). Gel-purified PCR products were subjected to Sanger sequencing, and resulting chromatograms were analyzed using TIDE (Tracking of Indels by Sequence Decomposition)[34].

Author Manuscript Author Manuscript Author Manuscript Author Manuscript

Luciferase reporter assays—Luciferase reporter assays were conducted using 3T3-[Shh-BlastR;Cas9] cells co-transfected with pGL3-8xGli-Firefly-luciferase and pGL3-SV40-Renilla-luciferase. One day after plating, cells were transfected using Mirus TransIT-2020 (Mirus Bio) with luciferase plasmids and either control GFP-encoding plasmid (pEF5B-FRT-GFP-FKBP)[86] or a plasmid encoding a gene of interest. Nearly confluent cells were switched to serum starvation medium with or without pathway agonist 24 h later, and allowed to signal for 24–30 h. Alternatively, luciferase assays for titering ShhN-conditioned medium were performed with the NIH-3T3 Light-II cell line, which has stably integrated versions of GLI-driven firefly luciferase and constitutively expressed Renilla luciferase. After signaling, cells were lysed in lysis buffer (12.5 mM Tris pH 7.4, 4% glycerol, 0.5% Triton X-100, 0.5 mg/mL BSA, 1 mM EGTA, 1 mM DTT) and a dual luciferase measurement performed using a Modulus microplate luminometer (Turner Biosystems).

Immunofluorescence and localization studies—IMCD3 FlpIn or 3T3-[Shh-BlastR;Cas9] cells were plated on acid-washed 13mm round #1.5 coverslips (additionally coated with poly-L-lysine for NIH-3T3 cells). After 24 h, cells were transfected as needed with siRNAs (Supplementary Table 9) using Lipofectamine RNAiMAX (Thermo Fisher) or with plasmids using Fugene 6 (Promega). Where indicated, cells were serum starved for 24 h and treated with ShhN or 1 μM vismodegib (Chemietek) before fixation using 4% paraformaldehyde, ice-cold methanol, or both in succession. For GLI2/GLI3/SMO trafficking assays, cells were serum-starved for 20 h, followed by 5–6 h incubation in the presence or absence of ShhN-conditioned medium. For analysis of TEDC2-LAP localization, cells were pre-extracted prior to methanol fixation via a one-minute exposure to PHEM buffer (60 mM PIPES, 25 mM HEPES, 4 mM $MgSO_4$, 10 mM EGTA, pH 7.0) with 0.2% TritonX-100.

Fixed coverslips were blocked using PBS with 3% BSA and 5% normal donkey serum, permeabilized using PBS with 0.1% Triton X-100, and then incubated with appropriate primary and secondary antibodies (Supplementary Table 10). Coverslips were either stained with Hoechst DNA dye and mounted on slides using Fluoromount-G mounting medium (Electron Microscopy Sciences) or directly mounted using ProLong Gold antifade reagent with DAPI (Life Technologies).

Coverslips were imaged at 60x or 63x magnification using one of the following microscope systems: an Axio Imager.M1 (Carl Zeiss) equipped with SlideBook software, an LED light source (Intelligent Imaging Innovations) and a Prime 95b sCMOS camera (Photometrics); an Axio Imager.M1 (Carl Zeiss) equipped with SlideBook software, a Lambda XL light source (Sutter instruments) and CoolSNAP HQ^2 CCD camera (Photometrics); an Axio Imager.M2 equipped with ZEN software, an X-Cite 120 LED light source (Excelitas) and an Axiocam 503 mono camera (Carl Zeiss); or a DeltaVision Elite imaging system equipped with SoftWoRx software, an LED light source, and sCMOS camera (Applied Precision). Z-stacks were acquired at 250–500 nm intervals and deconvolved as needed using Slidebook 6.0 or SoftWoRx softwares.

Author Manuscript Author Manuscript Author Manuscript Author Manuscript

Co-transfection and co-immunoprecipitation—HEK293T cells were co-transfected with *Tedc1*, *Tedc2* or *TagRFP* plasmids using Fugene 6, collected after 48 h, and lysed on ice in CoIP buffer (50 mM Tris pH 7.4, 150 mM NaCl, 1% Triton X-100, 1X DTT, 1X LPB) supplemented with protease inhibitors. Lysates were centrifuged at 20,000 × *g* for 20 min, and FLAG-tagged proteins were captured by incubation for 2 h with anti-FLAG M2 antibody (Sigma Aldrich) and Protein G Sepharose 4 Fast Flow (GE Healthcare). After four washes of resin with CoIP buffer, bound proteins were eluted by incubation at 95°C in lithium dodecyl sulfate-based gel loading buffer.

Western blotting—Lysates from 3T3-[Shh-BlastR;Cas9] cells were prepared in SDS sample buffer (50 mM Tris HCl pH 6.8, 8% v/v glycerol, 2% w/v SDS, 100 mM DTT, 0.1 mg/mL bromophenol blue), boiled and sonicated. Samples were loaded onto a 4–15% Criterion TGX Stainfree gel (Bio-Rad), and run for 25 min, 300V in Tris/Glycine/SDS buffer (Bio-Rad), before being transferred onto a PVDF membrane using a Transblot Turbo system (Bio-Rad). Membranes were blocked in 1:1 PBS:SeaBlock (Thermo Scientific) for 1 h at room temperature, and subsequently incubated with the indicated primary antibody for 16 h at 4 °C (Supplementary Table 10). After incubation with HRP-conjugated secondary antibody, blots were developed using Supersignal West Femto Maximum Sensitivity Substrate (Thermo Fisher) and imaged on a ChemiDoc MP (Bio-Rad). Membranes were stripped using Restore Western Blot stripping buffer (Thermo-Fisher) and re-probed as described.

For analysis of immunoprecipitations, Western blotting was performed as described above, except samples were separated in 4–12% Bis-Tris PAGE gels (Invitrogen) using MOPS running buffer, transferred to PVDF membranes using the Criterion Blotter system (Bio-Rad), developed using ECL or ECL 2 chemiluminescence detection kits (Pierce), and imaged on a Chemidoc Touch system (Bio-Rad).

Large-scale affinity purification and mass spectrometry—Affinity purifications were conducted as described[83]. Briefly, ~500–1000 µl packed cell volume was lysed in LAP purification buffer containing 0.3% NP-40. Lysate was cleared sequentially at 16,000 × *g* and 100,000 × *g* before incubation with anti-GFP antibody coupled to Protein A resin. After protein capture and washes, bound LAP-tagged proteins were eluted by incubation with HRV3C protease. For mass spectrometry analysis ‘A’ (see Supplementary Table 6), eluted proteins were further purified by capture on S-Protein agarose followed by elution at 95°C in lithium dodecyl sulfate-based gel loading buffer.

For protein analysis by mass spectrometry, gel slices containing affinity-purified proteins were washed with 50 mM ammonium bicarbonate, followed by reduction with DTT (5 mM) and alkylation using propionamide (10 mM). Gel slices were further washed with an acetonitrile-ammonium bicarbonate buffer until all stain was removed. 120 ng of Trypsin/LysC (Promega) reconstituted in 0.1% ProteaseMAX (Promega) with 50 mM ammonium bicarbonate was added to each gel band; after 30 min., 20 µL of additional 50 mM ammonium bicarbonate in 0.1% ProteaseMAX was added. Digestion was then allowed to occur overnight at 37 °C. Peptides were extracted from the gels in duplicate followed by drying using a SpeedVac concentrator. Peptide pools were then reconstituted and injected

Author Manuscript Author Manuscript Author Manuscript Author Manuscript

onto a C18 reversed phase analytical column, ~20 cm in length, pulled and packed in-house. The UPLC was a NanoAcquity or M-Class column (Waters), operated at 450 nL/min using a linear gradient from 4% mobile phase B to 45% B. Mobile phase A consisted of 0.2% formic acid, water; mobile phase B was 0.2% acetic acid, acetonitrile. The mass spectrometer was an Orbitrap Elite or Fusion (Thermo Fisher) set to acquire in a data-dependent fashion selecting and fragmenting the 15 most intense precursor ions in the ion-trap, where the exclusion window was set at 45 seconds and multiple charge states of the same ion were allowed.

QUANTIFICATION AND STATISTICAL ANALYSIS

Analysis of CRISPR-based screens—CRISPR-based screens were analyzed as described[26], processing data from each screen batch separately. To determine sgRNA counts in each sample, raw sequencing reads were trimmed to the 3′-most 17 nt of each protospacer and aligned to expected sgRNA sequences. This alignment was carried out with the makeCounts script of the casTLE software package[26], which uses Bowtie[87] to perform alignment with zero mismatches tolerated. The analyzeCounts script (v0.7 and v1.0) of casTLE was then used to identify genes exhibiting significant enrichment or depletion and to estimate the phenotypic effect size for each gene. This method uses an empirical Bayesian approach to score genes according to the log-likelihood ratio that a gene's observed changes in sgRNA counts is drawn from a model of gene effect versus the distribution of negative control sgRNAs. An expected negative score distribution is obtained by random permutation of gene-targeting sgRNA fold-change values and used to determine a *P* value for each gene. Note that the use of 100,000 permutations leads to a minimum reported *P* value of 1×10^{-5} (200,000 permutations were used for comparative screening in Supplementary Fig. 3c, with minimum *P* value of 5×10^{-6}). For each gene, the casTLE algorithm also estimates the magnitude of the phenotype resulting from complete gene inactivation. This value is output as the effect size and is accompanied by an estimated range of effect sizes compatible with each gene's sgRNA data.

Genes targeted by our sgRNA library that lacked an NCBI identifier or that severely affected growth (casTLE effect size ≤ −2.5 and casTLE *P* value < 0.005) were not considered for further analysis but are included in Supplementary Table 3. Negative and positive reference genes were defined for growth and signaling phenotypes using previously defined gene sets (Supplementary Table 3)[8,27]. Precision-recall and ROC curves were computed in Matlab (Mathworks). Hit genes at 10% and 20% false discovery rate cutoffs were defined using the precision-recall threshold values at precision of 0.9 and 0.8, yielding *P* value cutoffs of 0.0163 and 0.0338, respectively. Ciliopathy-associated genes were defined from OMIM. Functional category enrichment analysis for 10% FDR hits was performed using the DAVID website's Functional Annotation Chart tool using all mouse genes as the background[28]. A second analysis was performed using human homologs of 10% FDR hits using all human genes as the background. Significance of overlap between the top 15 congenital heart defect genes reported by Sifrim et al.[50] and *P* values from functional screening was assessed using the Kolmogorov-Smirnov test.

Author Manuscript Author Manuscript Author Manuscript Author Manuscript

Quantification of Hh signaling assays—Blasticidin-based inhibition of cell growth was determined by normalizing raw CellTiter-Blue fluorescence such that growth in the absence of blasticidin corresponds to 100% growth. The IC_{50} for blasticidin was determined using Prism 7.0 (Graphpad Software).

Dual-luciferase data were analyzed by first subtracting background signal such that cells without luciferase give readings of zero. Firefly to Renilla (8x-Gli to constitutive) ratios were then calculated and normalized such that unstimulated control cells have a value equal to 1.

Quantification of fluorescence microscopy images—Microscopy images were analyzed using Fiji ImageJ software (National Institutes of Health) and a custom Matlab (Mathworks) script. Local background subtraction was performed on all images before analysis. To determine ciliary frequency, cells were manually scored for the presence or absence of a cilium using ARL13B and acetylated tubulin as ciliary markers. For analyses of ciliary length and intensity of ciliary markers, the ARL13B and/or acetylated tubulin channels were used to create a ciliary mask. The ciliary mask was then used to determine cilium length and measure ciliary signal in other channels. The γ-tubulin or ninein signal (staining centrioles) was used to orient cilia from base to tip. Tip fluorescence for GLI2 and GLI3 was defined as the summed fluorescence in the distal-most five pixels of each cilium. For ARMC9-FLAG localization, the ciliary fluorescence of each cilium was normalized to 1, and each axoneme was divided in 20 equal-distance bins.

Differences in cilium length distribution were tested for significance using the Kolmogorov-Smirnov test in Matlab. Line plots of fluorescence intensity along cilia were generated in ImageJ.

Centriole counting measurements were done manually using γ-tubulin and centrin3 staining to guide centriole calling. Cell cycle stage was determined using DNA morphology, and statistical significance was determined using Fisher's exact test. Cell counts for each of the five centriole number categories were used for statistical comparisons between genotypes.

Analysis of mass spectrometry data—MS/MS data were analyzed using both Preview and Byonic v2.10.5 (ProteinMetrics). All data were first analyzed in Preview to provide recalibration criteria if necessary and then reformatted to MGF format before full analysis with Byonic. Data were searched at 12 ppm mass tolerances for precursors, with 0.4 Da fragment mass tolerances assuming up to two missed cleavages and allowing for fully specific and ragged tryptic peptides. The database used was Uniprot for *Mus musculus* downloaded on 10/25/2016. These data were validated at a 1% false discovery rate using typical reverse-decoy techniques[88]. The resulting identified peptide spectral matches and assigned proteins were then exported for further analysis using MatLab (MathWorks) to provide visualization and statistical characterization.

Analysis of CRISPR growth screen datasets—Gene-level growth phenotype data[74] were downloaded from the Achilles website. Hierarchical clustering using uncentered

Author Manuscript Author Manuscript Author Manuscript Author Manuscript

correlation and average linkage settings was performed using Cluster 3.0 software[89], and clustered data were visualized in Java Treeview[90].

Phylogenetic analysis—Homologs for *Tubd1* and *Tube1* were either previously described [91] or identified using protein BLAST. Homologs for *Tedc1* and *Tedc2* were identified using iterative searches with PSI-BLAST[92]. To analyze sequence divergence, homolog sequences were first aligned using Clustal Omega[93]. Phylogenetic trees were generated via neighbor joining with distance correction using Simple Phylogeny [93] and visualized using Unrooted[94].

Statistical analysis of centriole number—Tests of statistical significance for differences in centriole number between conditions were calculated by two-sided Fisher's exact test using Stata 14.2 (StataCorp).

CODE AVAILABILITY STATEMENT

Software used for casTLE analysis can be found at http://bitbucket.org/dmorgens/castle. Matlab scripts for quantification of cilium intensities and length are available upon request.

DATA AVAILABILITY STATEMENT

The data supporting the findings of this study are available within the paper and its Supplementary Information files, with the exception of raw Illumina sequencing data and sequencing-based analysis of CRISPR-induced mutations, which are available upon request.

Supplementary Material

Refer to Web version on PubMed Central for supplementary material.

Acknowledgments

We acknowledge members of the Chen and Nachury labs for advice and technical support; S. van Dorp for assistance with image quantification; P. Beachy (Stanford) for NIH-3T3 cells, 8xGli-luciferase reporter plasmid, and ShhN-producing HEK293T cells; K. Anderson (Sloan Kettering) for SMO antibody; G. Crabtree, K.C. Garcia, and A. Pyle for use of plate readers; N. Dimitrova for microscope use; C. Bustamante for use of an Illumina sequencer; R. Rohatgi (Stanford) for antibodies to EVC and IQCE; J. Wang and T. Stearns (Stanford) for sharing unpublished results and cDNA for *Cby1*; and M. Scott for helpful discussions. This project was supported by NIH Pathway to Independence Award K99/R00 HD082280 (D.K.B), Damon Runyon Dale F. Frey Award DFS-11-14 (D.K.B.), a seed grant from the Stanford Center for Systems Biology (D.K.B., S.H. and G.T.H.) and Stanford ChEM-H (M.C.B.), an NWO Rubicon Postdoctoral Fellowship (S.H.), National Science Foundation Graduate Research Fellowship DGE-114747 (D.W.M.), a Walter V. and Idun Berry Award (K.H.), T32 HG000044 (G.T.H.), DP2 HD08406901 (M.C.B.), R01 GM113100 (J.K.C.), and R01 GM089933 (M.V.N.). Cell sorting/flow cytometry was done on instruments in the Stanford Shared FACS Facility, including an instrument supported by NIH shared instrument grant S10RR025518-01. Mass spectrometry analyses were conducted in the Vincent Coates Foundation Mass Spectrometry Laboratory, Stanford University Mass Spectrometry and the Stanford Cancer Institute Proteomics/Mass Spectrometry Shared Resource; these centers are supported by Award S10 RR027425 from the National Center for Research Resources and NIH P30 CA124435, respectively. We thank Carsten Carstens, Ben Borgo, Peter Sheffield, and Laurakay Bruhn of Agilent Technologies for cilia-focused oligonucleotide sub-libraries.

References

1. Goetz SC, Anderson KV. The primary cilium: a signalling centre during vertebrate development. Nat Rev Genet. 2010; 11:331–44. [PubMed: 20395968]

Author Manuscript Author Manuscript Author Manuscript Author Manuscript

2. Nachury MV. How do cilia organize signalling cascades? Philos Trans R Soc Lond B Biol Sci. 2014; 369:20130465–20130465. [PubMed: 25047619]
3. Bangs F, Anderson KV. Primary Cilia and Mammalian Hedgehog Signaling. Cold Spring Harb Perspect Biol. 2017; 9
4. Braun DA, Hildebrandt F. Ciliopathies. Cold Spring Harb Perspect Biol. 2017; 9:a028191. [PubMed: 27793968]
5. Akizu N, et al. Mutations in CSPP1 lead to classical Joubert syndrome. Am J Hum Genet. 2014; 94:80–6. [PubMed: 24360807]
6. Wu F, Zhang Y, Sun B, McMahon AP, Wang Y. Hedgehog Signaling: From Basic Biology to Cancer Therapy. Cell Chem Biol. 2017; 24:252–280. [PubMed: 28286127]
7. Pak E, Segal RA. Hedgehog Signal Transduction: Key Players, Oncogenic Drivers, and Cancer Therapy. Dev Cell. 2016; 38:333–44. [PubMed: 27554855]
8. Roosing S, et al. Functional genome-wide siRNA screen identifies KIAA0586 as mutated in Joubert syndrome. Elife. 2015; 4:e06602. [PubMed: 26026149]
9. Wheway G, et al. An siRNA-based functional genomics screen for the identification of regulators of ciliogenesis and ciliopathy genes. Nat Cell Biol. 2015; 17:1074–87. [PubMed: 26167768]
10. Jacob LS, et al. Genome-wide RNAi screen reveals disease-associated genes that are common to Hedgehog and Wnt signaling. Sci Signal. 2011; 4:ra4. [PubMed: 21266715]
11. Kim J, et al. Functional genomic screen for modulators of ciliogenesis and cilium length. Nature. 2010; 464:1048–51. [PubMed: 20393563]
12. Shalem O, et al. Genome-scale CRISPR-Cas9 knockout screening in human cells. Science. 2014; 343:84–7. [PubMed: 24336571]
13. Koike-Yusa H, Li Y, Tan EP, del Velasco-Herrera MC, Yusa K. Genome-wide recessive genetic screening in mammalian cells with a lentiviral CRISPR-guide RNA library. Nat Biotechnol. 2014; 32:267–73. [PubMed: 24535568]
14. Wang T, Wei JJ, Sabatini DM, Lander ES. Genetic screens in human cells using the CRISPR-Cas9 system. Science. 2014; 343:80–4. [PubMed: 24336569]
15. Zhou Y, et al. High-throughput screening of a CRISPR/Cas9 library for functional genomics in human cells. Nature. 2014; 509:487–91. [PubMed: 24717434]
16. Deans RM, et al. Parallel shRNA and CRISPR-Cas9 screens enable antiviral drug target identification. Nat Chem Biol. 2016; 12:361–6. [PubMed: 27018887]
17. Wang T, et al. Identification and characterization of essential genes in the human genome. Science. 2015; 350:1096–101. [PubMed: 26472758]
18. Wang T, et al. Gene Essentiality Profiling Reveals Gene Networks and Synthetic Lethal Interactions with Oncogenic Ras. Cell. 2017; 168:890–903. e15. [PubMed: 28162770]
19. Hart T, et al. High-Resolution CRISPR Screens Reveal Fitness Genes and Genotype-Specific Cancer Liabilities. Cell. 2015; 163:1515–1526. [PubMed: 26627737]
20. Tzelepis K, et al. A CRISPR Dropout Screen Identifies Genetic Vulnerabilities and Therapeutic Targets in Acute Myeloid Leukemia. Cell Rep. 2016; 17:1193–1205. [PubMed: 27760321]
21. Orchard RC, et al. Discovery of a proteinaceous cellular receptor for a norovirus. Science. 2016; 353:933–6. [PubMed: 27540007]
22. Park RJ, et al. A genome-wide CRISPR screen identifies a restricted set of HIV host dependency factors. Nat Genet. 2017; 49:193–203. [PubMed: 27992415]
23. Arroyo JD, et al. A Genome-wide CRISPR Death Screen Identifies Genes Essential for Oxidative Phosphorylation. Cell Metab. 2016; 24:875–885. [PubMed: 27667664]
24. Taipale J, et al. Effects of oncogenic mutations in Smoothened and Patched can be reversed by cyclopamine. Nature. 2000; 406:1005–9. [PubMed: 10984056]
25. Morgens DW, et al. Genome-scale measurement of off-target activity using Cas9 toxicity in high-throughput screens. Nat Commun. 2017; 8:15178. [PubMed: 28474669]
26. Morgens DW, Deans RM, Li A, Bassik MC. Systematic comparison of CRISPR/Cas9 and RNAi screens for essential genes. Nat Biotechnol. 2016; 34:634–6. [PubMed: 27159373]

Author Manuscript Author Manuscript Author Manuscript Author Manuscript

27. Hart T, Brown KR, Sircoulomb F, Rottapel R, Moffat J. Measuring error rates in genomic perturbation screens: gold standards for human functional genomics. Mol Syst Biol. 2014; 10:733. [PubMed: 24987113]
28. Huang DW, Sherman BT, Lempicki RA. Systematic and integrative analysis of large gene lists using DAVID bioinformatics resources. Nat Protoc. 2009; 4:44–57. [PubMed: 19131956]
29. Webb TR, et al. Diphthamide modification of eEF2 requires a J-domain protein and is essential for normal development. J Cell Sci. 2008; 121:3140–5. [PubMed: 18765564]
30. Chen CM, Behringer RR. Ovca1 regulates cell proliferation, embryonic development, and tumorigenesis. Genes Dev. 2004; 18:320–32. [PubMed: 14744934]
31. Loucks CM, et al. Matching two independent cohorts validates DPH1 as a gene responsible for autosomal recessive intellectual disability with short stature, craniofacial, and ectodermal anomalies. Hum Mutat. 2015; 36:1015–1019. [PubMed: 26220823]
32. Allen BL, et al. Overlapping roles and collective requirement for the coreceptors GAS1, CDO, and BOC in SHH pathway function. Dev Cell. 2011; 20:775–87. [PubMed: 21664576]
33. Izzi L, et al. Boc and Gas1 each form distinct Shh receptor complexes with Ptch1 and are required for Shh-mediated cell proliferation. Dev Cell. 2011; 20:788–801. [PubMed: 21664577]
34. Brinkman EK, Chen T, Amendola M, van Steensel B. Easy quantitative assessment of genome editing by sequence trace decomposition. Nucleic Acids Res. 2014; 42:e168. [PubMed: 25300484]
35. Lee YL, et al. Cby1 promotes Ahi1 recruitment to a ring-shaped domain at the centriole-cilium interface and facilitates proper cilium formation and function. Mol Biol Cell. 2014; 25:2919–33. [PubMed: 25103236]
36. Burke MC, et al. Chibby promotes ciliary vesicle formation and basal body docking during airway cell differentiation. The Journal of cell biology. 2014; 207:123–137. [PubMed: 25313408]
37. Glazer AM, et al. The Zn finger protein Iguana impacts Hedgehog signaling by promoting ciliogenesis. Dev Biol. 2010; 337:148–56. [PubMed: 19852954]
38. Li FQ, et al. BAR Domain-Containing FAM92 Proteins Interact with Chibby1 To Facilitate Ciliogenesis. Mol Cell Biol. 2016; 36:2668–2680. [PubMed: 27528616]
39. Dorn KV, Hughes CE, Rohatgi R. A Smoothened-Evc2 complex transduces the Hedgehog signal at primary cilia. Dev Cell. 2012; 23:823–35. [PubMed: 22981989]
40. Pusapati GV, et al. EFCAB7 and IQCE regulate hedgehog signaling by tethering the EVC-EVC2 complex to the base of primary cilia. Dev Cell. 2014; 28:483–96. [PubMed: 24582806]
41. Ruiz-Perez VL, Goodship JA. Ellis-van Creveld syndrome and Weyers acrodental dysostosis are caused by cilia-mediated diminished response to hedgehog ligands. Am J Med Genet C Semin Med Genet. 2009; 151C:341–51. [PubMed: 19876929]
42. Shaheen R, et al. Genomic analysis of Meckel-Gruber syndrome in Arabs reveals marked genetic heterogeneity and novel candidate genes. Eur J Hum Genet. 2013; 21:762–8. [PubMed: 23169490]
43. Shaheen R, et al. Characterizing the morbid genome of ciliopathies. Genome Biol. 2016; 17:242. [PubMed: 27894351]
44. Kar A, Phadke SR, Das Bhowmik A, Dalal A. Whole exome sequencing reveals a mutation in ARMC9 as a cause of mental retardation, ptosis and polydactyly. bioRxiv. 2017:109124.
45. Panigrahi I, Phadke SR, Agarwal SS. Mental retardation, ptosis and polydactyly: a new autosomal recessive syndrome? Clin Dysmorphol. 2002; 11:289–92. [PubMed: 12401996]
46. Nager AR, et al. An Actin Network Dispatches Ciliary GPCRs into Extracellular Vesicles to Modulate Signaling. Cell. 2017; 168:252–263.e14. [PubMed: 28017328]
47. Phua SC, et al. Dynamic Remodeling of Membrane Composition Drives Cell Cycle through Primary Cilia Excision. Cell. 2017; 168:264–279 e15. [PubMed: 28086093]
48. Van De Weghe JC, et al. Mutations in ARMC9, which Encodes a Basal Body Protein, Cause Joubert Syndrome in Humans and Ciliopathy Phenotypes in Zebrafish. Am J Hum Genet. 2017; 101:23–36. [PubMed: 28625504]
49. Xu M, et al. Mutations in the Spliceosome Component CWC27 Cause Retinal Degeneration with or without Additional Developmental Anomalies. Am J Hum Genet. 2017; 100:592–604. [PubMed: 28285769]

Author Manuscript Author Manuscript Author Manuscript Author Manuscript

50. Sifrim A, et al. Distinct genetic architectures for syndromic and nonsyndromic congenital heart defects identified by exome sequencing. Nat Genet. 2016; 48:1060–5. [PubMed: 27479907]
51. Oegema R, et al. Human mutations in integrator complex subunits link transcriptome integrity to brain development. PLoS Genet. 2017; 13:e1006809. [PubMed: 28542170]
52. Sollis E, et al. Identification and functional characterization of de novo FOXP1 variants provides novel insights into the etiology of neurodevelopmental disorder. Hum Mol Genet. 2016; 25:546–57. [PubMed: 26647308]
53. Comartin D, et al. CEP120 and SPICE1 cooperate with CPAP in centriole elongation. Curr Biol. 2013; 23:1360–6. [PubMed: 23810536]
54. Lin YN, et al. CEP120 interacts with CPAP and positively regulates centriole elongation. J Cell Biol. 2013; 202:211–9. [PubMed: 23857771]
55. Mahjoub MR, Xie Z, Stearns T. Cep120 is asymmetrically localized to the daughter centriole and is essential for centriole assembly. J Cell Biol. 2010; 191:331–46. [PubMed: 20956381]
56. Kanie T, et al. The CEP19-RABL2 GTPase Complex Binds IFT-B to Initiate Intraflagellar Transport at the Ciliary Base. Dev Cell. 2017; 42:22–36 e12. [PubMed: 28625565]
57. Mojarad BA, et al. CEP19 cooperates with FOP and CEP350 to drive early steps in the ciliogenesis programme. Open Biol. 2017; 7
58. Nishijima Y, et al. RABL2 interacts with the intraflagellar transport-B complex and CEP19 and participates in ciliary assembly. Mol Biol Cell. 2017; 28:1652–1666. [PubMed: 28428259]
59. Gupta GD, et al. A Dynamic Protein Interaction Landscape of the Human Centrosome-Cilium Interface. Cell. 2015; 163:1484–99. [PubMed: 26638075]
60. Jakobsen L, et al. Novel asymmetrically localizing components of human centrosomes identified by complementary proteomics methods. EMBO J. 2011; 30:1520–35. [PubMed: 21399614]
61. Knorz VJ, et al. Centriolar association of ALMS1 and likely centrosomal functions of the ALMS motif-containing proteins C10orf90 and KIAA1731. Mol Biol Cell. 2010; 21:3617–29. [PubMed: 20844083]
62. Izquierdo D, Wang WJ, Uryu K, Tsou MF. Stabilization of cartwheel-less centrioles for duplication requires CEP295-mediated centriole-to-centrosome conversion. Cell Rep. 2014; 8:957–65. [PubMed: 25131205]
63. Chang P, Stearns T. Delta-tubulin and epsilon-tubulin: two new human centrosomal tubulins reveal new aspects of centrosome structure and function. Nat Cell Biol. 2000; 2:30–5. [PubMed: 10620804]
64. Dupuis-Williams P, et al. Functional role of epsilon-tubulin in the assembly of the centriolar microtubule scaffold. J Cell Biol. 2002; 158:1183–93. [PubMed: 12356863]
65. Dutcher SK, Morrissette NS, Preble AM, Rackley C, Stanga J. Epsilon-tubulin is an essential component of the centriole. Mol Biol Cell. 2002; 13:3859–69. [PubMed: 12429830]
66. O'Toole ET, Giddings TH, McIntosh JR, Dutcher SK. Three-dimensional organization of basal bodies from wild-type and delta-tubulin deletion strains of Chlamydomonas reinhardtii. Mol Biol Cell. 2003; 14:2999–3012. [PubMed: 12857881]
67. Ross I, Clarissa C, Giddings TH Jr, Winey M. epsilon-tubulin is essential in Tetrahymena thermophila for the assembly and stability of basal bodies. J Cell Sci. 2013; 126:3441–51. [PubMed: 23704354]
68. Sharma A, et al. Centriolar CPAP/SAS-4 Imparts Slow Processive Microtubule Growth. Dev Cell. 2016; 37:362–76. [PubMed: 27219064]
69. Schmidt TI, et al. Control of centriole length by CPAP and CP110. Curr Biol. 2009; 19:1005–11. [PubMed: 19481458]
70. Kirkham M, Muller-Reichert T, Oegema K, Grill S, Hyman AA. SAS-4 is a C. elegans centriolar protein that controls centrosome size. Cell. 2003; 112:575–87. [PubMed: 12600319]
71. Hein MY, et al. A human interactome in three quantitative dimensions organized by stoichiometries and abundances. Cell. 2015; 163:712–23. [PubMed: 26496610]
72. Huttlin EL, et al. Architecture of the human interactome defines protein communities and disease networks. Nature. 2017; 545:505–509. [PubMed: 28514442]

Author Manuscript Author Manuscript Author Manuscript Author Manuscript

73. Wong YL, et al. Cell biology. Reversible centriole depletion with an inhibitor of Polo-like kinase 4. Science. 2015; 348:1155–60. [PubMed: 25931445]
74. Aguirre AJ, et al. Genomic Copy Number Dictates a Gene-Independent Cell Response to CRISPR/Cas9 Targeting. Cancer Discov. 2016; 6:914–29. [PubMed: 27260156]
75. Wang JT, Kong D, Hoerner CR, Loncarek J, Stearns T. Centriole triplet microtubules are required for stable centriole formation and inheritance in human cells. Elife. 2017; 6
76. Li Y, et al. Global genetic analysis in mice unveils central role for cilia in congenital heart disease. Nature. 2015; 521:520–4. [PubMed: 25807483]
77. MacArthur DG, et al. Guidelines for investigating causality of sequence variants in human disease. Nature. 2014; 508:469–76. [PubMed: 24759409]
78. Wang JT, Kong D, Hoerner CR, Loncarek J, Stearns T. Centriole triplet microtubules are required for stable centriole formation and inheritance in human cells. bioRxiv. 2017
79. Pimenta-Marques A, et al. A mechanism for the elimination of the female gamete centrosome in Drosophila melanogaster. Science. 2016; 353:aaf4866. [PubMed: 27229142]
80. Zheng X, et al. Molecular basis for CPAP-tubulin interaction in controlling centriolar and ciliary length. Nat Commun. 2016; 7:11874. [PubMed: 27306797]
81. Bond J, et al. A centrosomal mechanism involving CDK5RAP2 and CENPJ controls brain size. Nat Genet. 2005; 37:353–5. [PubMed: 15793586]
82. Gilmore EC, Walsh CA. Genetic causes of microcephaly and lessons for neuronal development. Wiley Interdiscip Rev Dev Biol. 2013; 2:461–78. [PubMed: 24014418]
83. Liew GM, et al. The intraflagellar transport protein IFT27 promotes BBSome exit from cilia through the GTPase ARL6/BBS3. Dev Cell. 2014; 31:265–78. [PubMed: 25443296]
84. Frank-Kamenetsky M, et al. Small-molecule modulators of Hedgehog signaling: identification and characterization of Smoothened agonists and antagonists. J Biol. 2002; 1:10. [PubMed: 12437772]
85. Chen JK, Taipale J, Young KE, Maiti T, Beachy PA. Small molecule modulation of Smoothened activity. Proc Natl Acad Sci U S A. 2002; 99:14071–6. [PubMed: 12391318]
86. Breslow DK, Koslover EF, Seydel F, Spakowitz AJ, Nachury MV. An in vitro assay for entry into cilia reveals unique properties of the soluble diffusion barrier. J Cell Biol. 2013; 203:129–47. [PubMed: 24100294]
87. Langmead B, Trapnell C, Pop M, Salzberg SL. Ultrafast and memory-efficient alignment of short DNA sequences to the human genome. Genome Biol. 2009; 10:R25. [PubMed: 19261174]
88. Elias JE, Gygi SP. Target-decoy search strategy for increased confidence in large-scale protein identifications by mass spectrometry. Nat Methods. 2007; 4:207–14. [PubMed: 17327847]
89. de Hoon MJ, Imoto S, Nolan J, Miyano S. Open source clustering software. Bioinformatics. 2004; 20:1453–4. [PubMed: 14871861]
90. Saldanha AJ. Java Treeview--extensible visualization of microarray data. Bioinformatics. 2004; 20:3246–8. [PubMed: 15180930]
91. Turk E, et al. Zeta-Tubulin Is a Member of a Conserved Tubulin Module and Is a Component of the Centriolar Basal Foot in Multiciliated Cells. Curr Biol. 2015; 25:2177–83. [PubMed: 26234217]
92. Altschul SF, et al. Gapped BLAST and PSI-BLAST: a new generation of protein database search programs. Nucleic Acids Res. 1997; 25:3389–402. [PubMed: 9254694]
93. Li W, et al. The EMBL-EBI bioinformatics web and programmatic tools framework. Nucleic Acids Res. 2015; 43:W580–4. [PubMed: 25845596]
94. Perrière G, Gouy M. WWW-query: an on-line retrieval system for biological sequence banks. Biochimie. 1996; 78:364–369. [PubMed: 8905155]

Author Manuscript Author Manuscript Author Manuscript Author Manuscript

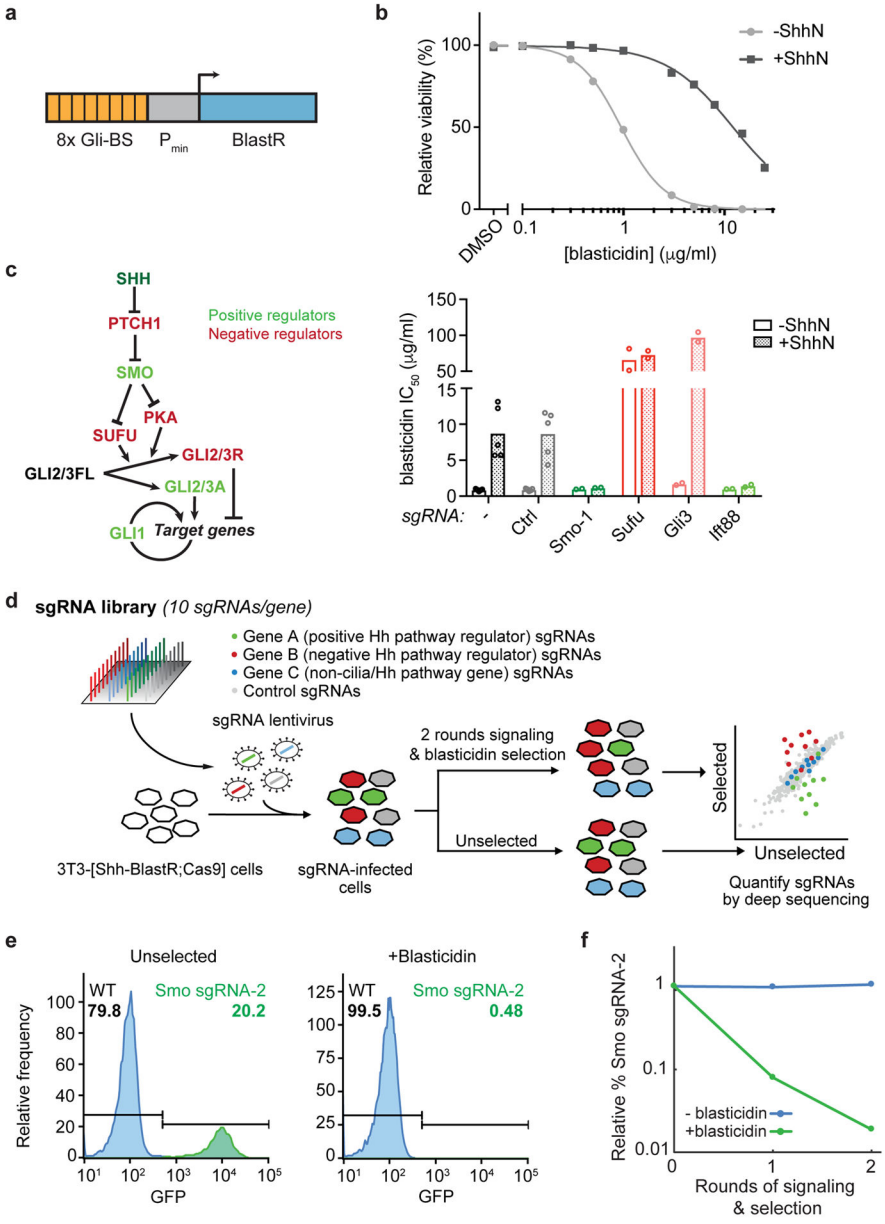

Figure 1. Development of a Hedgehog pathway reporter-based screening strategy

a) A transcriptional reporter combining 8 copies of the GLI binding sequence (Gli-BS) with a minimal promoter (P_{min}) to convert Hh signals into blasticidin resistance. **b)** Blasticidin resistance was assayed across a range of concentrations in stimulated (+ShhN) and unstimulated 3T3-[Shh-BlastR;Cas9] cells. Representative curves of 5 independent experiments performed in duplicate. **c**) Overview of the Hh pathway, with key negative and positive regulators shown in red and green, respectively (left). Effects of control sgRNAs on blasticidin resistance in stimulated and unstimulated 3T3-[Shh-BlastR;Cas9] cells (right). Bars show mean inhibitory concentration 50 (IC_{50}) values and circles show IC_{50} values from N = 2 (for gene-targeting sgRNAs) or 5 (for no sgRNA and negative control (Ctrl) sgRNA) independent experiments performed in duplicate. **d**) Overview of the screening strategy.

Author Manuscript Author Manuscript Author Manuscript Author Manuscript

Cells receiving a negative control sgRNA, a positive regulator-targeting sgRNA, and a negative regulator-targeting sgRNA are shaded grey, green, and red, respectively. **e**) Flow cytometry histograms of cell mixtures showing the fraction of GFP positive (Smo sgRNA-2, green) cells either in the absence of selection (left) or after two rounds of signaling and selection (right). Representative results from three independent experiments. **f**) Quantification of cell depletion as in (**e**).

Author Manuscript Author Manuscript Author Manuscript Author Manuscript

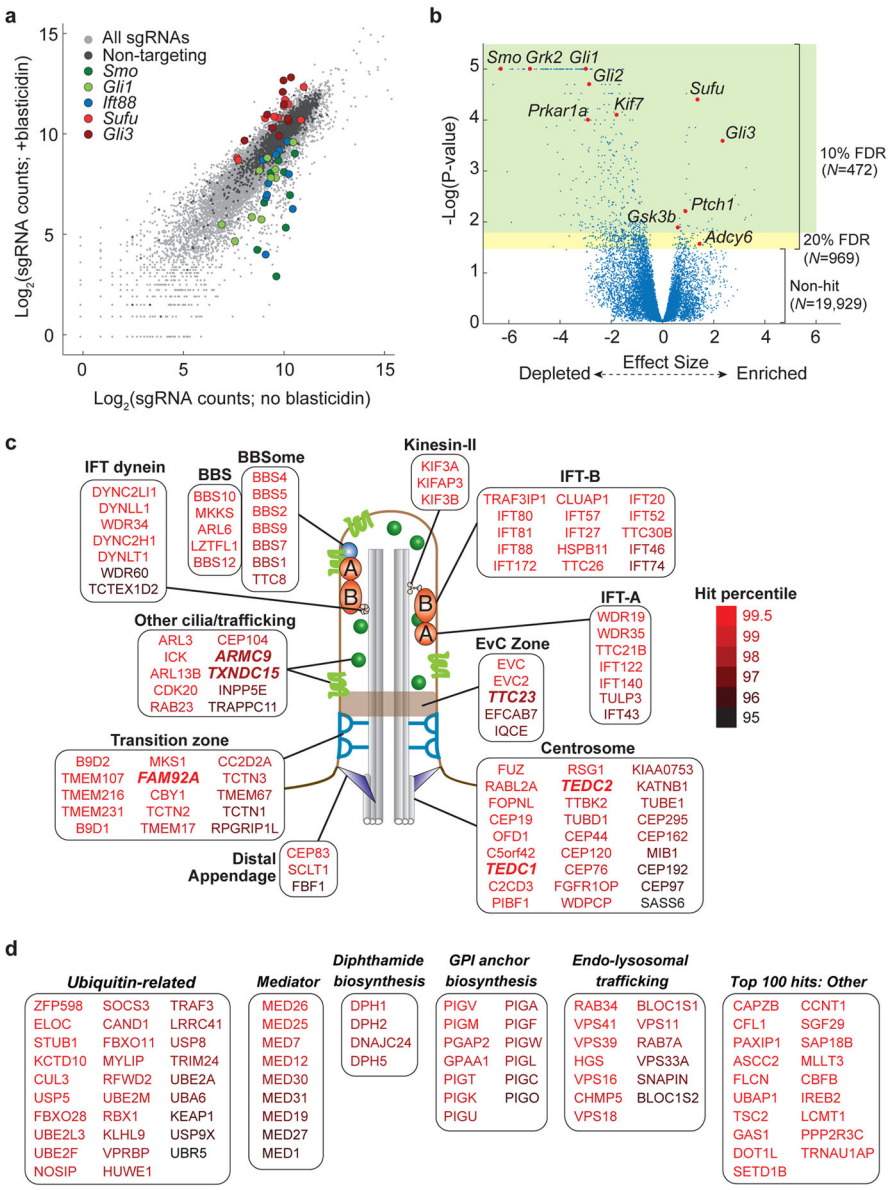

Figure 2. Overview of genome-wide screen results

a) Scatter plot showing $\log_2$ of normalized sgRNA counts in selected versus unselected cell pools, with sgRNAs targeting select genes highlighted. **b**) Volcano plot of casTLE *P* values versus effect sizes for all genes (after filtering; see **Methods**), with select Hh pathway components highlighted. Green area indicates *P*-value cutoff corresponding to 10% false discovery rate (FDR); combined green and yellow areas indicate 20% FDR, with the number of genes in each area indicated. **c**) Schematic illustration of a primary cilium, with known structural features and select protein products of hit genes shown. Proteins shown are grouped by protein complex membership or localization, with select newly identified hits highlighted in bold, italic font. **d**) For the indicated categories, proteins encoded by hit genes identified are listed in order of statistical confidence. In addition to select gene ontology

terms enriched among screen hits, the top 100 hits not otherwise listed in panels a–c are shown.

Author Manuscript Author Manuscript Author Manuscript Author Manuscript

Author Manuscript Author Manuscript Author Manuscript Author Manuscript

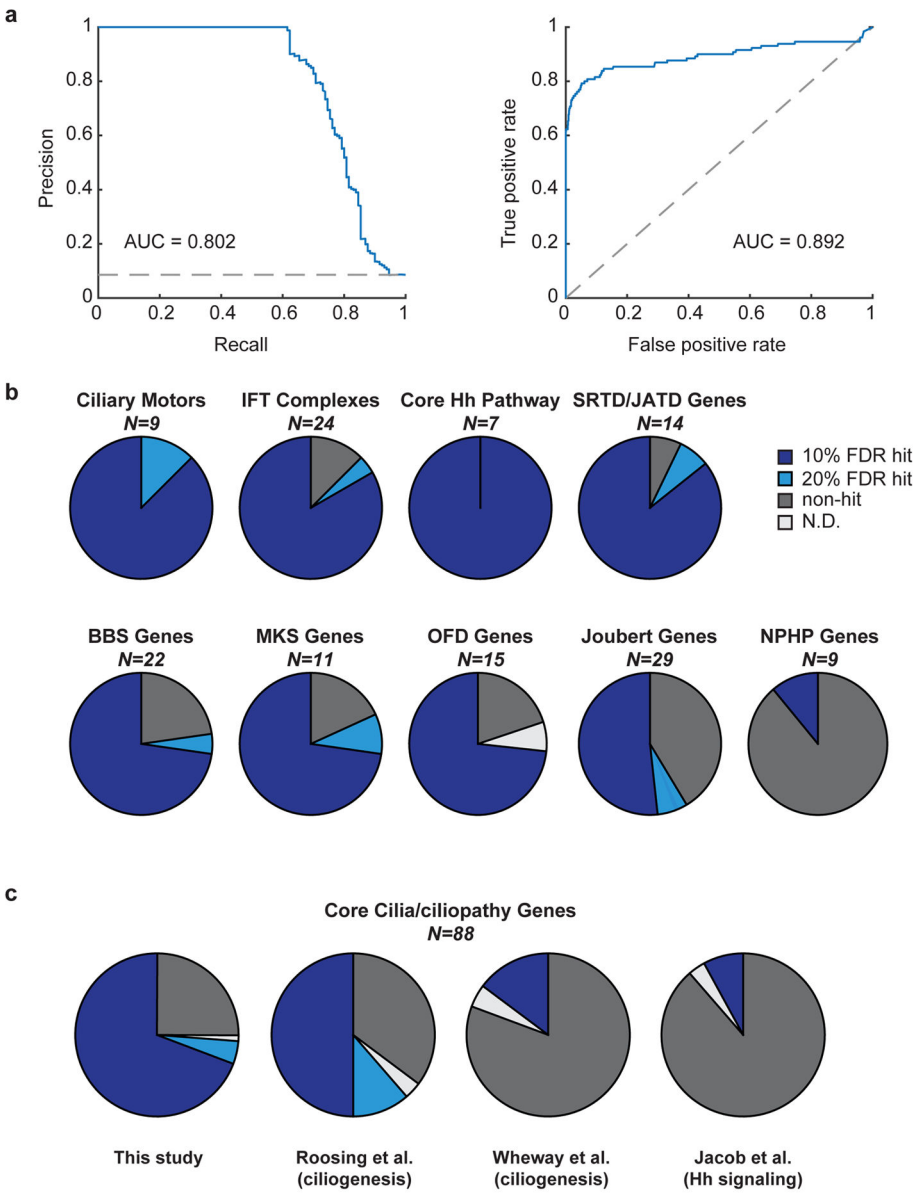

Figure 3. Evaluation of screen performance

a) Assessment of screen performance using 130 positive and 1386 negative reference genes, as determined by precision-recall analysis (left) and ROC curve (right), with the area under each curve (AUC) shown. Dashed lines indicate performance of a random classification model. **b**) Analysis of hit gene detection for select gene categories (N = number of genes in each category), with the fraction of hits detected at 10% or 20% FDR, not detected, or not determined shown; see Supplementary Table 3 for details. The NPHP category includes genes mutated exclusively in NPHP and not other ciliopathies. Abbreviations: SRTD (short rib thoracic dysplasia), JATD (Jeune asphyxiating thoracic dysplasia), OFD (Oral-Facial-Digital Syndrome). **c**) Hit gene identification is compared for the indicated datasets. Pie charts show the fraction of N=88 genes detected as hits across all genes included in part (**b**),

except the NPHP-specific category; see Supplementary Fig. 3a for detail among individual categories.

Author Manuscript Author Manuscript Author Manuscript Author Manuscript

Author Manuscript Author Manuscript Author Manuscript Author Manuscript

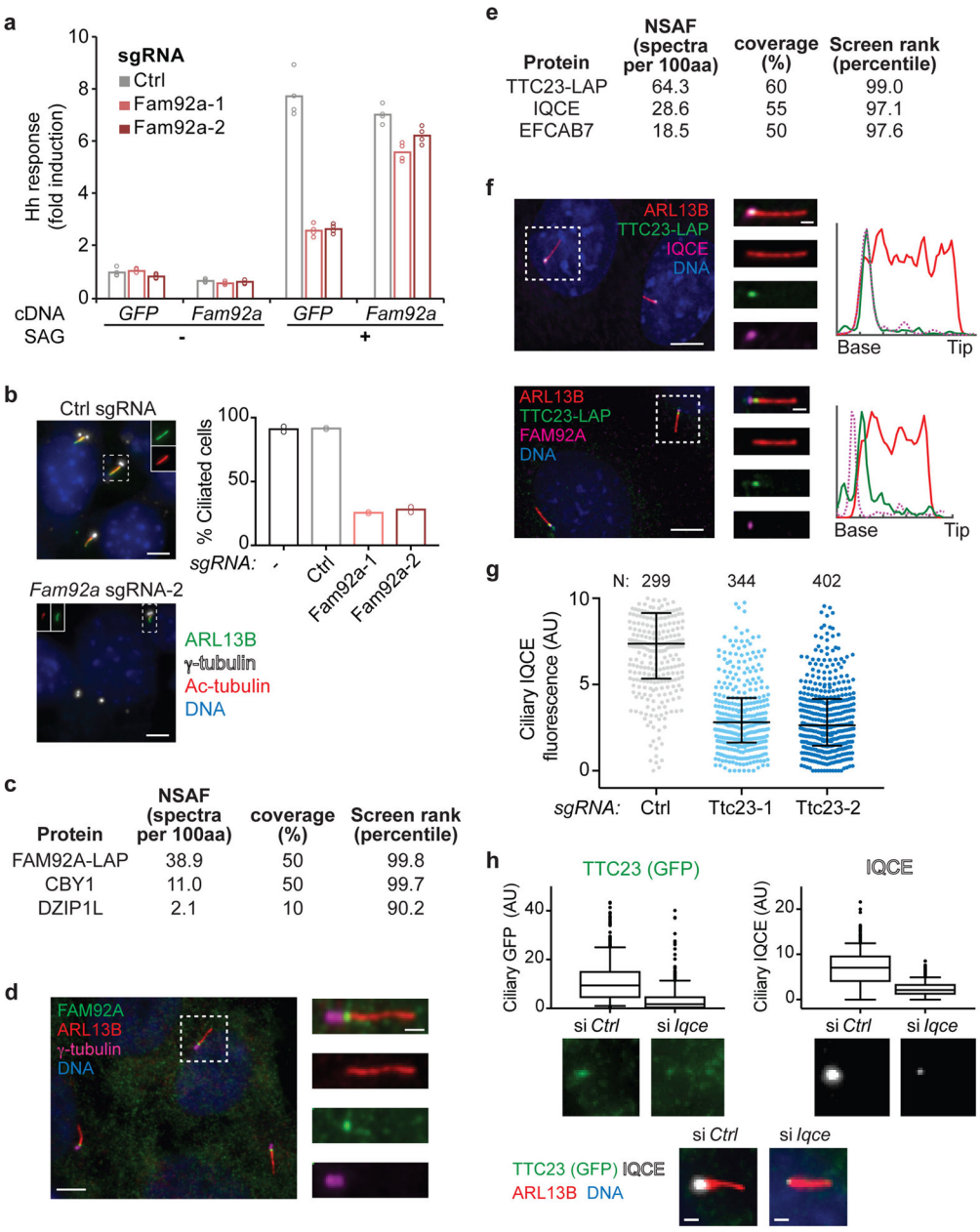

Figure 4. Characterization of FAM92A and TTC23 as transition zone and EvC zone components

a) Induction of Hh pathway luciferase reporter is shown for cells transduced with the indicated sgRNAs and transfected with plasmids encoding *Fam92a-3xFLAG* (*Fam92a*) or *GFP-FKBP* (*GFP*). Cells were untreated or stimulated with SAG. Bars show mean of 4 replicate measurements (circles); one of two representative experiments. **b**) Analysis of cilia in 3T3-[Shh-BlastR;Cas9] cells transduced with the indicated sgRNAs. Bars show mean percentage of ciliated cells; dots show ciliated percentage in each of two independent experiments (>200 cells analyzed per datapoint). Scale bar: 5 μm **c**) Mass spectrometry analysis of FAM92A-associated proteins purified from IMCD3 cells. The normalized spectral abundance factor (NSAF), the percent of each protein covered by identified

Author Manuscript Author Manuscript Author Manuscript Author Manuscript

peptides, and the percentile rank of the corresponding gene in the screen are indicated. **d**) FAM92A localizes to the transition zone of IMCD3 cells, distal to centrioles (γ-tubulin) and proximal to the ciliary membrane (ARL13B). One of two independent experiments (five fields of view each). Scale bars: 5 μm and 1 μm (insets). **e**) Mass spectrometry analysis of TTC23-associated proteins purified from IMCD3 cells. **f**) TTC23-LAP co-localizes with IQCE, distal to FAM92A, in IMCD3 cells. Line plots show normalized intensity along the length of the cilium; tick marks are 1 μm intervals. Representative images are shown from two independent experiments (five fields of view each). Scale bars: 5 μm and 1 μm (insets). **g**) The median and interquartile range of ciliary IQCE levels are shown for cells transduced with the indicated sgRNAs; one of two independent experiments. **h**) Ciliary TTC23-LAP and IQCE signals were analyzed following introduction of *Iqce*-targeting or control (*Ctrl*) siRNAs. The median, interquartile range (box boundaries), 10–90% percentile range (whiskers), and outliers are plotted for N=390 (*Ctrl*) and N=300 (*Iqce*) cilia. One of two (IQCE) or four (GFP) replicate experiments. Scale bars: 1 μm.

Author Manuscript Author Manuscript Author Manuscript Author Manuscript

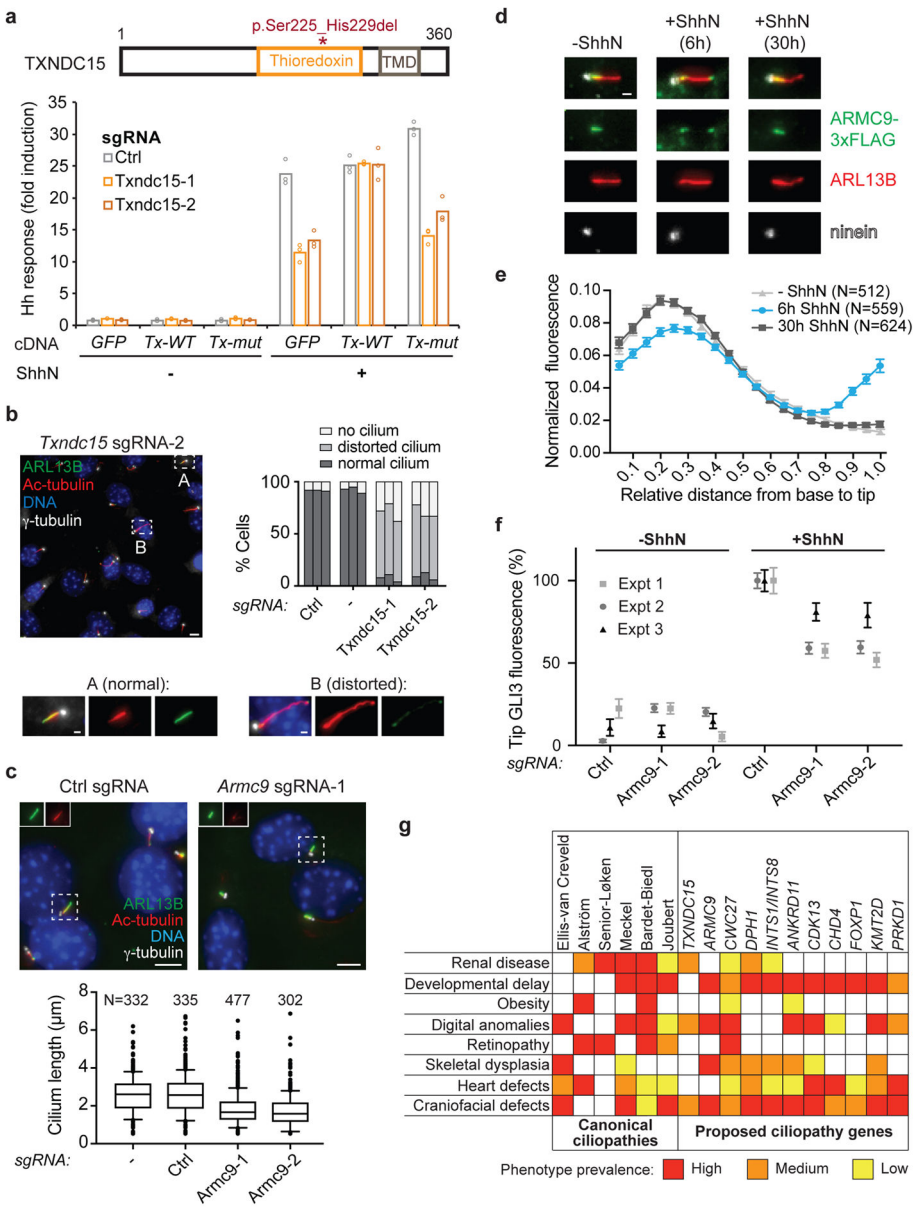

Figure 5. Insights into ciliopathies from previously uncharacterized screen hits

a) TXNDC15, with the transmembrane domain (TMD), thioredoxin domain, and MKS-associated mutation indicated (top). Luciferase reporter levels were measured for cells transduced with the indicated sgRNAs and transfected with plasmids encoding *GFP-FKBP (GFP)*, wildtype *Txndc15* (*Tx-WT*), or mutant *Txndc15* (*Tx-mut*). Bars show mean of 3 replicates (circles); one of two representative experiments. **b**) Cilia were analyzed in 3T3-[Shh-BlastR;Cas9] cells transduced with the indicated sgRNAs. Bars in graph show percentage of cells with cilia that are normal, distorted, or absent. Each bar per condition represents an independent experiments with >200 cells counted. Scale bars: 5 μm and 1 μm (insets). **c**) Cilia were analyzed in 3T3-[Shh-BlastR;Cas9] cells transduced with the indicated sgRNAs. Representative images are shown at top. At bottom, the median cilium length, interquartile range (box boundaries), 10–90% percentile range (whiskers), and

Author Manuscript Author Manuscript Author Manuscript Author Manuscript

outliers are plotted. One of three independent experiments. Scale bars: 5 μm. **d**) Analysis of ARMC9-FLAG localization relative to centrioles (ninein) and ciliary membrane (ARL13B) is shown for IMCD3 cells treated as indicated. Scale bar: 1 μm. **e**) ARMC-FLAG intensity along the length of the cilium from base (position 0) to tip (position 1.0) was measured for IMCD3 cells treated as indicated. The mean and standard deviation are plotted after normalizing the total intensity in each cilium to 1.0; one of three representative experiments. **f**) Fluorescence intensity of GLI3 at the cilium tip was measured for the indicated cells in the presence or absence of ShhN. Mean and standard error of the mean are shown for each of N=3 independent experiments (at least 250 cilia analyzed per condition). **g**) Table showing select clinical features in canonical ciliopathies and their observation in the context of specific mutations and syndromes. Colors indicate high (red), moderate (orange) and low (yellow) prevalence.

Author Manuscript Author Manuscript Author Manuscript Author Manuscript

a

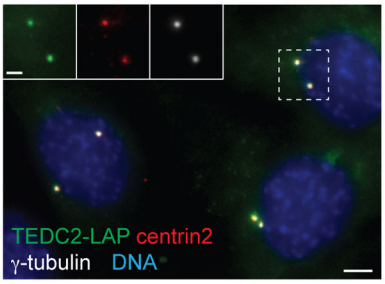

b

Protein	NSAF (spectra per 100aa)	coverage (%)	Screen rank (percentile)
TEDC2-LAP	46.8	76	99.5
TEDC1	47.1	73	99.8
TUBE1	32.6	61	98.7
TUBD1	30.3	60	99.4
TUBB5	14.4	54	lethal
TUBA1B	12.9	55	lethal
CENPJ	4.0	35	85.2

c

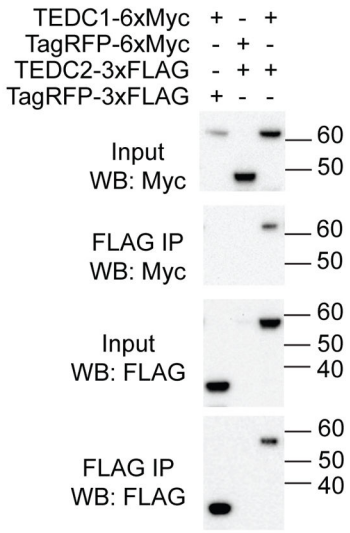

Figure 6. TEDC1 and TEDC2 form a tetrameric complex with δ- and ε-tubulins

a) IMCD3 cells stably expressing TEDC2-LAP were immunostained with antibodies to centrin2 and γ-tubulin to visualize centrioles. Scale bar: 5 μm (2 μm for insets). Representative images are shown for three independent experiments. **b**) Mass spectrometry analysis of TEDC2-associated proteins purified from IMCD3 cells reveals TEDC1, ε-tubulin, δ-tubulin in nearly stoichiometric amounts, as well as α/β-tubulin and CENPJ. For each protein, the normalized spectral abundance factor (NSAF), the percent of the protein covered by identified peptides, and the percentile rank of the corresponding gene in the screen dataset are indicated. **c**) Binding of TEDC1 and TEDC2 was assessed via co-immunoprecipitations performed in HEK293T cells transfected with plasmids encoding the indicated proteins. Recovered proteins were analyzed by Western blot. Representative blots are shown for two independent experiments. See also Supplementary Fig. 6b and Supplementary Fig. 8.

Author Manuscript Author Manuscript Author Manuscript Author Manuscript

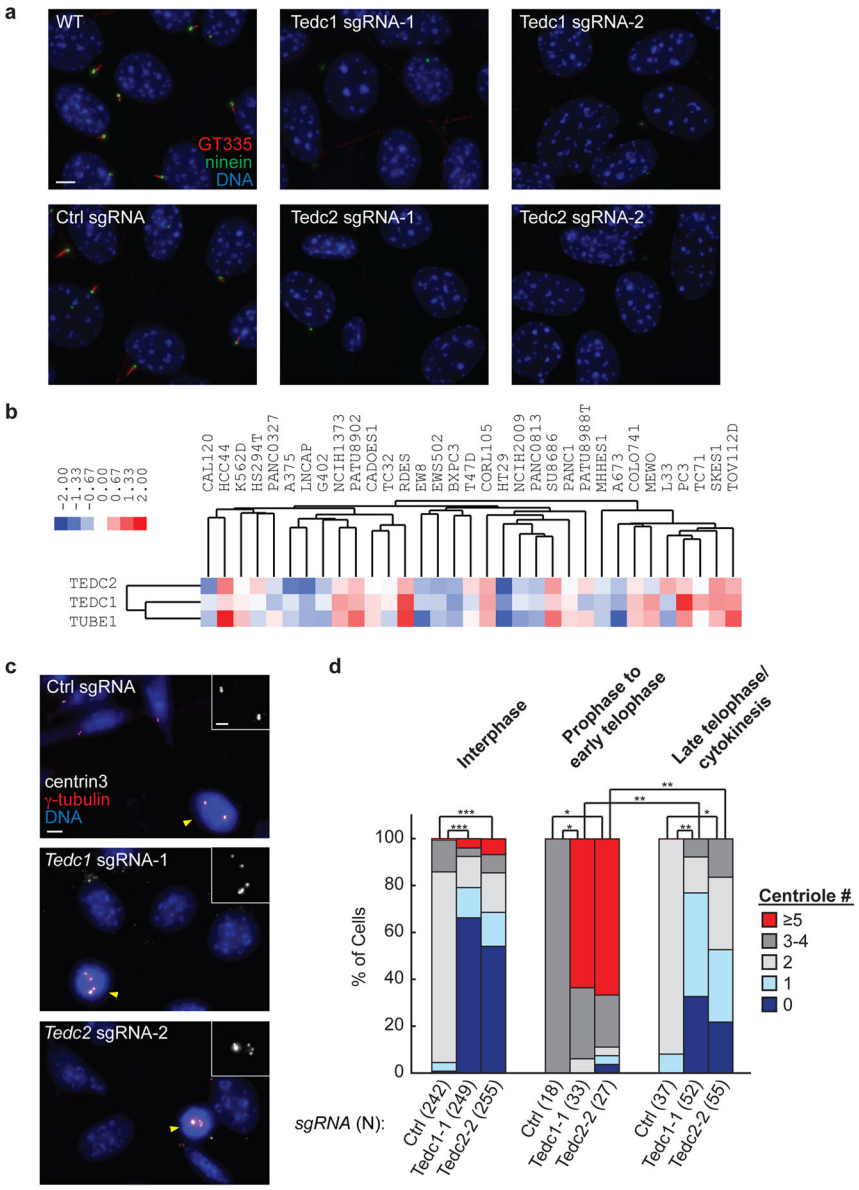

Figure 7. The TED complex is required for centriole stability

a) Cells transduced with the indicated sgRNAs were stained with antibodies to ninein (centrioles) and polyglutamylated tubulin (GT335, centrioles and cilia). Scale bar: 5 μm. One of three representative experiments. **b**) Hierarchical clustering of relative growth scores across the indicated cell lines reveals that *TEDC1*, *TEDC2*, and *TUBE1* share a similar pattern of relative fitness. Blue and red shading indicates decreased and increased proliferation relative to the average behavior across all cell lines. **c**) For cells transduced with the indicated sgRNAs, centrioles were visualized by staining with antibodies to centrin3 and γ-tubulin. Insets show centrin3 staining in mitotic cells, marked by yellow arrowheads. Scale bars: 5 μm (2 μm for insets). See also Supplementary Fig. 6h. One of three representative experiments. **d**) Centrioles marked by centrin3 and γ-tubulin were counted in cells at the indicated cell cycle stages. Statistically significant differences in centriole counts

are shown for select conditions (*, $P < 1\times10^{-6}$; **, $P < 1\times10^{-10}$; ***, $P < 1\times10^{-60}$, determined by two-sided Fisher's exact test).

Author Manuscript Author Manuscript Author Manuscript Author Manuscript